

Article

Rapid Immobilisation of Chemical Reactions in Alkali-Activated Materials Using Solely Microwave Irradiation

Anže Tesovnik ^{1,2}  and Barbara Horvat ^{3,*} 

¹ Slovenian National Building and Civil Engineering Institute, Dimičeva Ulica 12, 1000 Ljubljana, Slovenia; anze.tesovnik@zag.si

² Jožef Stefan International Postgraduate School, Jamova 39, 1000 Ljubljana, Slovenia

³ Milan Vidmar Electric Power Research Institute, Hajdrihova 2, 1000 Ljubljana, Slovenia

* Correspondence: barbara.horvat@eimv.si

Abstract: Efflorescence, a time-dependent and water-driven phenomenon, is a major concern in alkali-activated materials (AAMs), impacting their practical use and preservation in a time-frozen state for post-characterisation. Although a method for stopping chemical reactions in conventional cements exists, it is time-consuming and not chemical-free. Therefore, this study explored the effects of low-power microwave-induced dehydration on efflorescence, mechanical performance, and structural integrity in AAMs, to create an alternative and more “user-friendly” dehydration method. For this purpose, several mixtures based on secondary raw (slag, fly ash, glass wool, and rock wool) and non-waste (metakaolin) materials were activated with a commercial Na-silicate solution in ratios that promoted or prevented efflorescence. Characterisation techniques, including Fourier-transform infrared spectroscopy and X-ray diffraction, showed that microwave dehydration effectively removed water without altering crystallinity, while mercury intrusion porosimetry and compressive strength tests confirmed increased porosity. In addition to being an efficient, time-saving, and solvent-free manner of stopping the reactions in AAMs, microwave irradiation emerged as an innovative, chemical-free method for evaluating curing finalisation and engineering foams in a stage when all other existing methods fail. However, the artificially provoked efflorescence in aged dehydrated AAMs connected the slipperiness of AAM with the instant extraction of Na, which raised the need for further research into alternative alkali replacements to evaluate the practical use of AAM.

Keywords: alkali-activated materials; efflorescence; dehydration; microwave irradiation; stopping chemical reactions; curing completion



Citation: Tesovnik, A.; Horvat, B. Rapid Immobilisation of Chemical Reactions in Alkali-Activated Materials Using Solely Microwave Irradiation. *Minerals* **2024**, *14*, 1219. <https://doi.org/10.3390/min14121219>

Academic Editor: Elsabe Kearsley

Received: 4 October 2024

Revised: 10 November 2024

Accepted: 23 November 2024

Published: 29 November 2024



Copyright: © 2024 by the authors. Licensee MDPI, Basel, Switzerland. This article is an open access article distributed under the terms and conditions of the Creative Commons Attribution (CC BY) license (<https://creativecommons.org/licenses/by/4.0/>).

1. Introduction

The construction and civil engineering sectors, in conjunction with the cement production industry, are major contributors to global emissions. The prevailing linear economic model has resulted in a surge in natural resource consumption, global emissions, and waste accumulation. Cement, the most used manmade material in the world and the predominant material for the building and civil engineering sectors, contributes to approximately 8% of the world’s total CO₂ emissions through its manufacturing processes [1]. The estimated trend of increased percentage of urbanisation and building material usage [2] demands the research and development of a new generation of sustainable materials, with a specific focus on achieving a sustainable construction industry.

In recent decades, there has been a notable increase in the research dedicated to alkali-activated materials (AAMs), which are emerging as promising alternatives to ordinary Portland cement and industrial ceramics [1]. AAMs are cementitious materials formed from solid aluminosilicate precursors with sufficient amounts of Si and Al in amorphous content, which are then alkali-activated using an alkali silicate solution or hydroxides [3]. This alternative material, which can support the objectives of a circular economy, offers economic and environmental benefits, particularly through the reuse of waste materials [4–7].

As a source of precursors, industrial or agricultural wastes, such as slags, rock wool, glass wool, fly ash, waste glass powder residues, or biomass ashes, can be used to reduce the usage of raw materials in building and civil engineering production [8–14]. AAMs offer several advantages over conventional materials such as simple preparation, sustainability, potential lower cost, vast and versatile access to local precursor materials (different slags [15–21], ashes [10,22–27], metakaolin [28–31], mineral wools [16,17,32], refractory materials [33], foundry waste materials [34,35], green waste ceramics [36], clay-rich river sediments [37], etc.), lower production energy consumption, low hydration heat, freezing resistance [38], chemical resistance, strong durability, high strength [39], and excellent high-temperature stability. However, a major drawback of AAMs is their inclination toward the time-dependent evolution of the chemical–mineral composition, where the negative outcome is usually observed as efflorescence [40].

Efflorescence is an intrinsic phenomenon characterised by microstructural changes owing to leaching and carbonation of unreacted alkali cations, leaving behind salts [41]. In the context of AAMs, this phenomenon is attributable to either excess alkali serving as an activator or the dissolution of loosely bound materials, which facilitates the movement of soluble alkalis and the subsequent crystallisation of salts on the surface of the materials [42]. This natural process occurs under normal environmental conditions because of the high alkalinity and the tendency of alkalis to migrate within these substances [43]. Visible (common) white deposits, which are characteristic of efflorescence in AAMs, are a typical result of the carbonation of mobile alkalis. However, the presence of efflorescence in AAMs is undesirable because the leaching of calcium salts can reduce the mechanical strength and durability owing to structural degradation [44,45]. However, salts in AAMs typically contain sodium (Na) and are crystalline (thermonatrite, pirssonite, and different sodium carbonate salts [46]). This is because Na alkalis are the most used alkalis in AAM research [47]. When sodium silicate solution (Na_2SiO_3) is used as an activator, sodium-based salts can also form from free alkali ions [46]. Meanwhile, the silicon in Na_2SiO_3 primarily integrates into the amorphous gel structure [40,48], enhancing the binder's strength rather than precipitating as a separate salt phase. Sodium salts, however, can deteriorate the homogeneity and integrity of AAMs [49], making it desirable to minimise free Na in these materials. Moreover, efflorescence can be undesirable from an aesthetic and functional point of view.

Therefore, in formulations with reduced performance depending on the degree of carbonation, strategies can be implemented that reduce the rate of formation of carbonate species and CO_2 uptake. Lowering the alkali content in a material can diminish both the solubility and rate at which CO_2 is absorbed from the environment [50]. Choosing precursors or cement with a lower alkali content, that is, with a lower number of free alkali cations, can also minimise the risk of efflorescence [51]. Further, the optimisation of the curing conditions by adjusting the temperature and humidity can influence the release of active components and carbonation resistance [52], ultimately contributing to a reduction in efflorescence. Appropriate mix design and curing conditions can reduce the amount of free water available for the migration of alkali elements and salt formation. Further, to avoid efflorescence, the molar amount of elements accessible for the alkali activation reaction, found in the amorphous content, should follow the molar ratio $M:\text{Al} \leq 1$, where M represents the elements of the first group of the periodic system (PS), typically Na and K, provided that the alkalis from the second group of the PS are neglected and all amorphous elements dissolve in alkali [53].

However, the theoretical prediction of an ideal mixture is experimentally difficult [54]. Therefore, efflorescence as a time-dependent reaction, although delayed, occurs constantly and changes the chemical–mineralogical composition of the AAM [49,55]. These changes are due to the presence of water, which facilitates motion on the ionic–elemental scale in AAM. To hinder or even stop the reactions, the water content must be minimised or completely removed [43,55]. This is even more crucial when the chemical and mineralogical time evolution of the material under development is followed, because with certain

techniques (owing to their apparatus characteristics), all samples should preferably be measured simultaneously (aging of the X-ray tube when performing X-ray diffraction analysis [56]) and also re-measured later. Therefore, stopping the evolution of materials at preselected times is crucial to understand the design and control of materials in research [57].

The removal of water from the system should be complete and sufficiently rapid without the introduction of additional mechanical steps (such as milling) and solvents (such as isopropanol) [57–59]. This is to facilitate a decrease in the time required to reach the time-frozen state and avoid a potential influence on the chemistry and mineralogy of the material [57]. In addition, if the technique of water removal from the material is sufficiently rapid, different materials can be time-frozen at the same age. A comparison of the methods for dehydration or stopping hydration has mostly been performed using Portland cement. Solvent exchange with isopropanol is recommended by the International Union of Laboratories and Experts in Construction Materials, Systems and Structures (RILEM) as a stoppage method for phase assemblages in cement [60,61]. Isopropanol is weakly aggressive and may interact with the matrix. The interaction depends on the solubility of the material, its porosity, and the interaction between isopropanol and the alkali components of the matrix. Interactions between the material phases in cement and organic solvents have been reported [62–64]. With the recent increased interest in more environmentally friendly cementitious materials that exhibit chemical properties different from Portland cement, new research is required to assess proper drying methods. The isopropanol exchange method has been used in only a few studies to dry AAMs, with inconsistent results [59], while still requiring grinding of the material and prolonged time or heating to complete the evaporation of isopropanol [65].

Another technique for water removal is the induction of evaporation by heating the sample [66,67]. Conventional industrial ovens use electric heaters located at the top, bottom, or sides of the apparatus to increase the temperature in the chamber, where heat is conducted into the interior of the sample through the outer edges, resulting in uneven heating owing to the temperature gradient in the material [68–71]. Indirect heating through conduction and convection, which involves heating the air inside an oven and transferring heat to the sample, can result in higher energy consumption and may take longer depending on the sample size [69]. The longer the exposure time, the longer the time for changes in the chemical–mineral composition of the material. In the worst-case scenario, the outer layer of the heated bulk material may form a crustal structure that would hinder complete dehydration or lead to material explosion, owing to the inner pressures formed when water changes its state from liquid to gas. The procedure of dehydration to hinder unwanted reactions caused by the presence of water in the sample can be accomplished rapidly using a microwave oven where:

- The electromagnetic waves in the microwave region heat the sample volumetrically by influencing the dipoles of water molecules that are attempting to align with the rapidly changing electromagnetic field. This causes the water molecules to constantly rub the surrounding material, which increases the temperature owing to molecule-scale friction inside the bulk material [72].
- The electromagnetic field tends to affect the polarisability of water molecules even more in the presence of charged ions (Na and Cl) [73,74], which are present during alkali-activated synthesis. This accelerates heating and dehydration.
- Electromagnetic waves can be absorbed in the material, which additionally increases the temperature [75,76].

The process of heating a material with electromagnetic irradiation is volumetric on a large scale, with many randomly created heat sources inside the material on the molecular scale. By contrast, conventional heating in a convection oven involves surface heating, which requires more energy and time for dehydration.

The application of microwaves in the civil engineering sector has been demonstrated in several studies and exhibited a successful decrease in water content in building materials

using microwave irradiation. This has highlighted the potential application of microwave technology in building materials such as wood, bricks, and soil [77–81]. Nonetheless, research on the impact of microwaves on cement and AAMs remains limited. While the influence of microwaves on the curing process and mechanical strength has been investigated [53,82–88], the effect of post-curing microwave processing on AAMs and their dehydration has not yet been reported.

This study evaluated the effectiveness of post-curing low-power microwave irradiation in dehydrating various intact AAMs aiming to “freeze in time” chemical reactions without manual destruction of the samples. For this purpose, five different precursors (secondary waste materials like slag, fly ash, glass, and rock wool, as well as non-waste material metakaolin) were mixed in different ratios with a commercial Na-silicate solution. While microwave irradiation increased porosity, the shape of the pores defined whether the AAM was completely cured or would require more time or a higher curing temperature. To the best of our knowledge, this was reported for the first time and cannot be replaced by any conventional surface method. Irradiation-induced cracks became escape routes for the remnant water, which allowed excess alkali elements to accumulate on the surface. Fully cured samples, designed to avoid efflorescence, did not show early salt deposits, but dehydrated samples aged for a year after exposure to water did. Re-exposure to water caused immediate surface migration of Na, which explained the instant slipperiness of “to-water-exposed” AAMs. The study demonstrated that microwave irradiation can stop chemical reactions and efflorescence if the sample remains dry. However, due to increased porosity and reduced mechanical strength, this method is not suitable to heal already load-bearing products but may aid in post-characterisation purposes in material development and in the synthesis of permeable materials.

2. Materials and Methods

The precursors used in this study differed in all aspects to evaluate the validity of the effect of microwave irradiation until the complete dehydration of AAMs and draw overall conclusions. Therefore, the precursors were chemically and mineralogically analysed to theoretically predict the efflorescence ability of AAMs in the prepared mixtures.

2.1. Chemical and Mineralogical Characterisation of Precursors

Five different precursors were used for alkali activation: slag (SA), glass wool (GW), rock wool (RW), fly ash (FA), and metakaolin (MK). Except for MK, which is most commonly used in alkali activation and can be adopted as a standard, all the precursors represent locally obtained industrial waste. All precursors were dried (heating chamber WTB Binder, Binder GmbH, Tuttlingen, Germany, 70 °C for 24 h), milled (vibrating disk mill Siebtechnik TS250, Siebtechnik GmbH, Mülheim an der Ruhr, Germany), and sieved below 63 µm for X-ray fluorescence (XRF), X-ray diffraction (XRD), and Fourier-transform infrared spectroscopy (FTIR) analyses.

The mineralogical characteristics of the precursors were determined via XRD measurements (Empyrean PANalytical X-ray diffractometer, Malvern PANalytical, Malvern, UK, Cu X-ray source) in clean room conditions for angles 4–70° with a step size of 0.0263°. Powder samples were prepared in a back-loaded cylindrical sample holder with a diameter of 27 mm. Mineral analysis was performed using Rietveld refinement with the PANalytical X'Pert High Score Plus diffraction software (version 4.8, Malvern Panalytical, Surrey, UK). The amorphous content was evaluated employing an external standard method, as outlined by Madsen et al. [89], using α -Al₂O₃ powder (corundum, NIST676a, Gaithersburg, MD, USA) as the designated reference material.

The XRD patterns of the precursors used for the alkali activation and their mineral and amorphous content analyses are shown in Figure 1. The goodness of fit, ranging as 2.73–5.68, surpassed the ideal value of 1. However, this outcome was anticipated, considering that all the precursors comprised waste materials, with the exception of non-waste MK, which was not synthesised in the laboratory from pure substances. Therefore, the evaluation of

minerals in the secondary raw material as well as in the raw material exhibited difficulties in (i) not being able to explicitly determine the minerals (certain were barely detectable and certain exhibited overlapping peaks) and (ii) a significant amorphous halo.

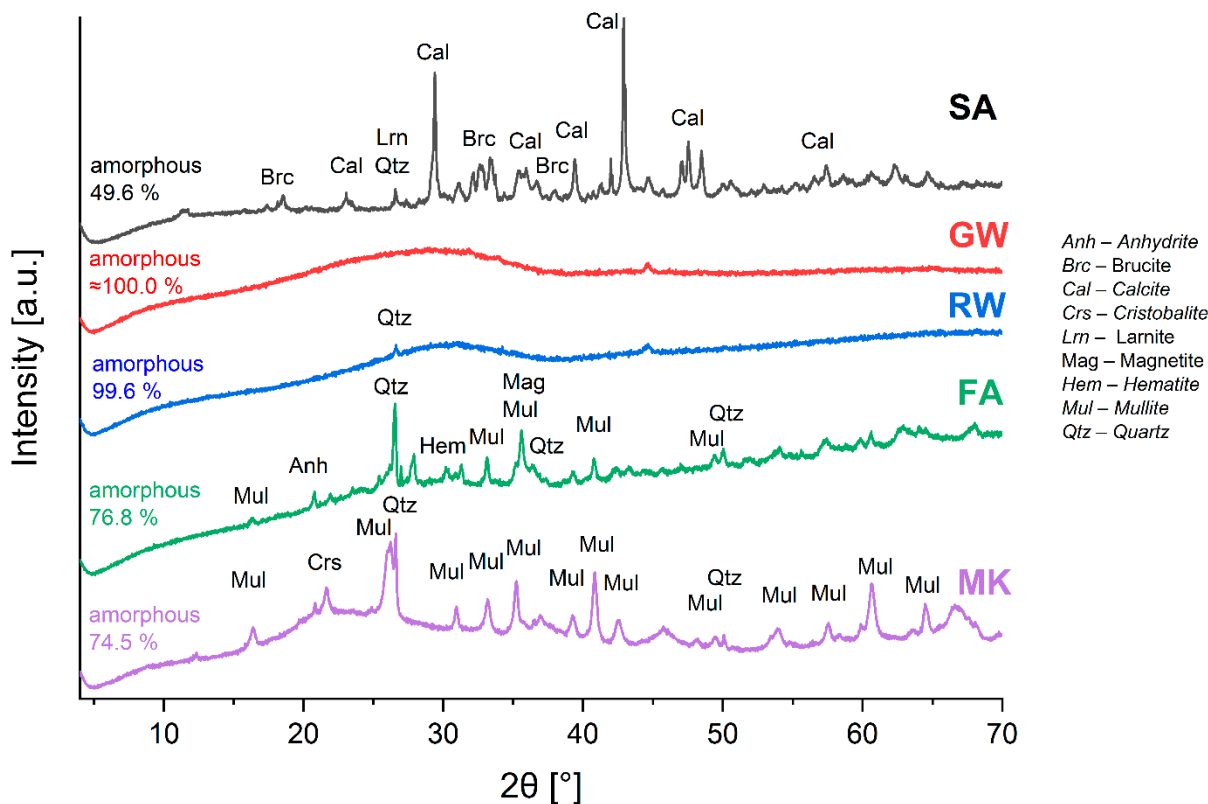


Figure 1. XRD patterns of precursors used in the study with determined minerals.

The GW and RW patterns exhibited a notably pronounced halo with a few smaller and less pronounced peaks. Thus, the GW and RW were almost completely amorphous (100 and 99.6%, respectively). For the other precursors, FA and MK contained approximately 75 m% of the amorphous phase, while SA contained about 50 m% (Figure 1). The overall determined amorphous content was as follows: GW \approx RW > FA \approx MK > SA. The minerals present in the precursors, their mass proportions, and chemical formulas are listed in Table S1.

Loss on ignition (LOI) was determined for dried powder samples by heating in a furnace (Nabertherm B 150, Lilienthal, Germany) at 550 °C for 2 h in an ambient atmosphere to remove organic compounds. Consequently, samples were heated again at 950 °C and for another 2 h to remove carbonates. The results were presented as mass loss relative to the initial mass of the sample before ignition.

The resulting ignited precursor samples were mixed with Fluxana_(s) (FX-X50-2, Li-tetraborate and Li-metaborate mixture, mass ratio 1:1; Sigma-Aldrich, St. Louis, MO, USA) at a mass ratio of 1:10, respectively, to lower the melting temperature during the formation of the molten discs. To avoid glueing the melt to the Pt crucible, LiBr_(l) (50 mL H₂O and 7.5 g of LiBr_(s) from Acros Organics, Antwerpen, Belgium) was added to the mixture. XRF analysis of the chemical composition was performed on the melted discs using a Thermo Scientific ARL Perform^X Sequential XRF spectrometer (Waltham, MA, USA), and the data were analysed using UniQuant 5 software (Thermo Fisher Scientific Inc., Waltham, MA, USA).

Table 1 presents the LOI results for the five tested (dry) precursors at temperatures of 550 °C (decomposition of an organic compound) and 950 °C (decomposition of carbonates). SA, GW, and RW had LOI values at 550 °C of approximately 5%. This suggested a higher

content of organic matter. FA and MK exhibited relatively low LOI values at 550 °C (0.7% and 1.3%, respectively), which was a consequence of the exposure to high temperatures during their production. SA had a significantly higher LOI at 950 °C (7.9%) than at 550 °C, which was attributed to the decomposition of carbonates (more than 10% of calcite was detected by XRD; Figure 1) [90]. GW and RW exhibited a decrease in LOI at 950 °C compared to that at 550 °C, which was attributed to the oxidation process (LOI was performed in the non-inert atmosphere). Further, FA and MK exhibited only a slight increase in LOI at 950 °C compared to that at 550 °C, which indicates that FA and MK have insignificant amounts of carbonates, if there are any at all (in crystalline form, there are none, according to XRD, Figure 1). According to Vdovin et al. [91], the increase in LOI at 950 °C is attributed to chemically bound water.

Table 1. Mass percentage of elements measured with XRF, elements in the crystalline form with XRD, and elements in the amorphous content (XRF–XRD).

Precursor	Elements [m%]	Na	K	Mg	Ca	Al	Si	LOI ^{550 °C}	LOI ^{950 °C}
SA	XRF	0	0.03	8.22	27.53	5.92	9.15	4.75	7.86
	XRD	0	0	2.86	15.32	0.48	4.26		
	XRF–XRD	0	0.03	5.36	12.22	5.44	4.89		
GW	XRF	10.01	0.39	3.39	6.2	3.21	29.14	5.74	3.85
	XRD	0.24	0.1	0	0	0	0.65		
	XRF–XRD	9.77	0.29	3.39	6.2	3.21	28.49		
RW	XRF	1.59	0.64	7.34	11.71	10.61	18.44	4.63	4.16
	XRD	0.12	0.05	0	0	0.16	0.28		
	XRF–XRD	1.47	0.59	7.34	11.71	10.45	18.16		
FA	XRF	0.68	2.04	1.53	6.34	14.08	20.4	0.74	0.82
	XRD	0.26	0	0	0.89	4.63	5.68		
	XRF–XRD	0.42	2.04	1.53	5.45	9.45	14.72		
MK	XRF	0	0.9	0.18	0.27	24.08	24.04	1.29	2.05
	XRD	0	0	0	0	7.19	5.13		
	XRF–XRD	0	0.9	0.18	0.27	16.89	18.91		

The chemical composition of the amorphous content of all precursors is presented in Table 1 and was determined from the XRF (all elements) and XRD (elements that are present in minerals) results according to the methodology described in a previous work [36]. The elements present in minerals (XRD) were deduced from elements measured by XRF.

FTIR (PerkinElmer Spectrum Two) was performed in ATR mode in the range of 380–4000 cm^{−1} on the precursors to identify the presence of chemical bonds.

The FTIR spectra of precursors are presented in Figure 2. Precursor SA exhibited a strong peak at 1417 cm^{−1}, which was attributed to the asymmetric stretching vibrations of the carbonate ions (CO₃^{2−}) in calcite (presence of calcite was determined also by XRD, Figure 2). The peaks at 874 and 712 cm^{−1} were also owing to calcite [92,93]. The peak observed at approximately 959 cm^{−1} was attributed to the T–O–Si asymmetric stretching vibration [94], where T can be either silicon (Si) or aluminium (Al). The presence of this non-sharp peak indicated that the slag also contained amorphous silicates/aluminosilicates required for alkali activation.

The GW spectrum showed broad and less sharp peaks owing to the amorphous nature of the precursor (as indicated by the XRD pattern in Figure 1). The broad peak at approximately 946 cm^{−1} was associated with the T–O–Si asymmetric stretching vibrations, which are characteristic of silica- or aluminosilica-based materials [94]. The peak at 774 cm^{−1} could be related to the bending vibrations of Si–O bonds, further suggesting the presence of silica structure [95].

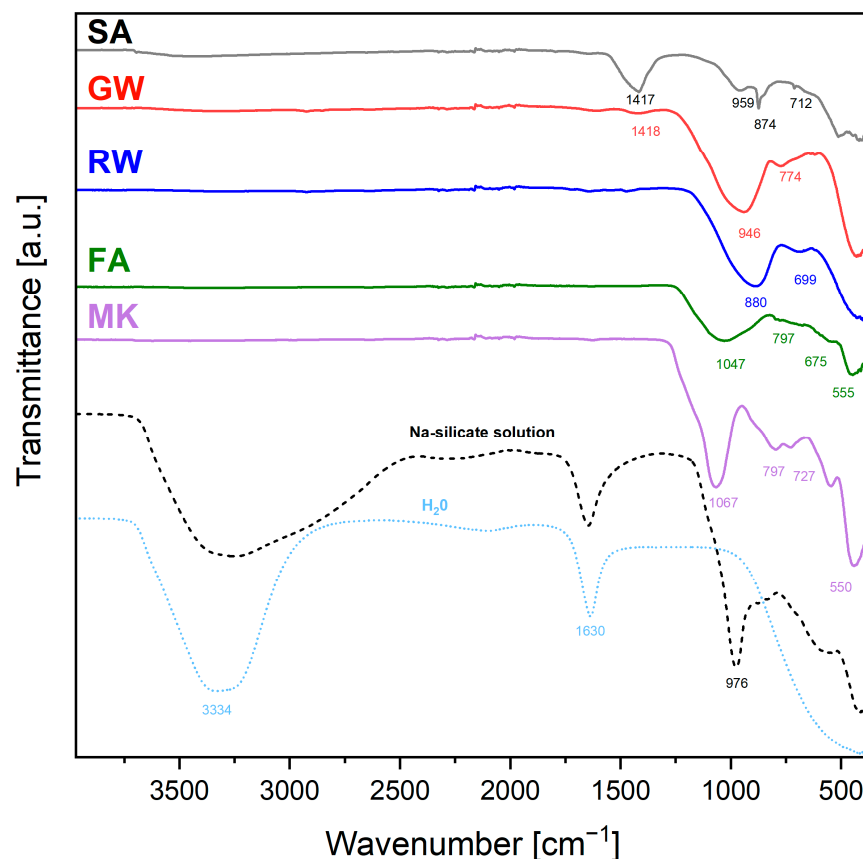


Figure 2. FTIR spectral analysis of precursors used in alkali activation. The dashed line shows the Na-silicate solution and the distilled water measurement to identify water peaks.

The FTIR spectrum of RW exhibited two distinct broad absorption peaks at wavenumbers 880 and 699 cm^{-1} . The peak at 880 cm^{-1} was associated with the T-Si-O asymmetric stretching vibration [96], and that at 699 cm^{-1} was related to the bending vibration of Si-O [97].

The most prominent peak in FA, with a minimum at 1047 cm^{-1} , was characteristic of the Si-O-Si asymmetric stretching vibrations. In the interval of 1253–826 cm^{-1} , a broad vibration of the T-O bond was observed, where the mullite, quartz, and glassy phases overlapped. A less prominent peak at 797 cm^{-1} was associated with the Si-O-Si bending vibrations [95,98]. The peaks at 675 and 555 cm^{-1} were related to the bending vibrations of the T-O-Si bonds [98,99], which further confirmed the existence of silicate or aluminosilicate structures in the FA.

The MK spectrum exhibited a well-defined peak with a minimum at 1067, 797, and 727 cm^{-1} representing Si-O-Si asymmetric stretching vibrations [100]. The peak at 550 cm^{-1} and the bands at 1253 and 826 cm^{-1} could be associated with the bending modes of the T-O-Si bonds [99,101], which is expected in metakaolin, a dehydroxylated form of kaolinite that contains aluminosilicate (mullite presence indicated by XRD, Figure 1).

Therefore, the only common parameter for all precursors is that they contain amorphous Al and Si, which indicates that they are potential sources for alkali activation synthesis.

The ingredient used in all experiments with all precursors was a Na-silicate solution, which had, in addition to water peaks (3334 and 1630 cm^{-1}), a peak at 976 cm^{-1} . Because the solution did not contain Al, the peak at 976 cm^{-1} was owing to Si-O asymmetric stretching vibrations.

2.2. Preparation and Evaluation of Precursors for Synthesis

To synthesise the AAMs, the MK and FA precursors were used as received without any additional treatment. However, RW and GW were processed by milling and sieving to

achieve a particle size below 63 μm . Further, SA was milled in large mass (2 kg) for 3 h in a ball mill (ball diameter 5 cm), and sieved to below 400 μm .

The particle size distribution (PSD) of the precursors was determined using laser diffraction granulometry (Microtrack MRB, Sync+TurboSync laser grain size analyser, Montgomeryville and York, PA, USA) under a dry-dispersion measurement setting.

The dried precursors without a conductive layer were evaluated using a scanning electron microscope (SEM; Jeol JSM-IT500, Tokyo, Japan) under low-vacuum conditions at an accelerating voltage of 20 kV to determine the particle shape of the precursors.

The SEM micrographs of the precursors, taken at magnifications of 100 \times and 500 \times , and the different sizes, shapes, and morphological aspects of the particles were visualised using SEM and are presented together with the results of PSD in Figure 3.

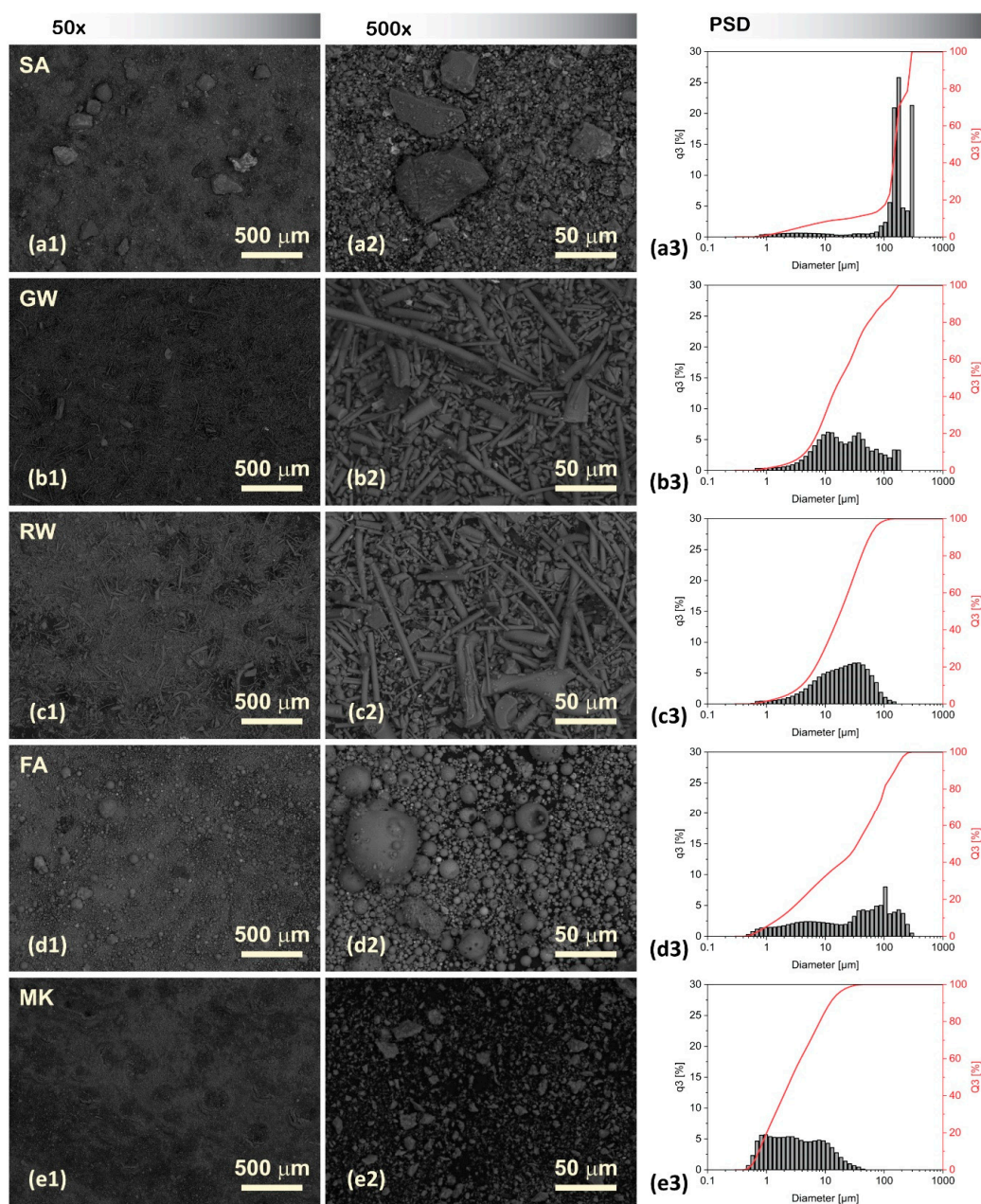


Figure 3. SEM micrographs of precursors at two magnifications: 100 (left column) and 500 (centre column), displaying the morphological differences between (a1,a2) SA, (b1,b2) GW, (c1,c2) RW, (d1,d2) FA, and (e1,e2) MK particles. In the (right column), the results of the particle size distribution (PSD) of the precursor are presented based on distribution histogram q3 and cumulative curve Q3.

The shapes of the precursors observed by SEM can provide valuable insights into their microstructural characteristics. The SA particles exhibited dense, irregular, and angular shapes with coarse surfaces as a result of grinding. The GW and RW exhibited an elongated structure with a smooth texture, which is typical for both fibrous insulation materials. The FA particles presented a wide distribution of spherical shapes of various sizes, indicating relatively uniform but diverse particulates. The surfaces of these particles were mostly smooth, with certain degrees of pitting. The MK exhibited a uniform distribution of fine particles with a relatively rough texture and angular shape.

Comparatively, the PSD analysis revealed that SA particles were the largest, followed in descending order by FA, GW, and RW, with the smallest particles observed in the case of MK. The mean diameters and main percentiles are listed in Supplementary Table S2.

Therefore, the trend from larger to smaller average particle sizes is based on the PSD as: SA > FA > GW > RW > MK.

2.3. Preparation of AAMs and Microwave Dehydration Treatment

Three mixtures were formulated for each waste precursor (SA, GW, RW, and FA), and for the non-waste MK, only two (workability of the slurry with the smallest amount of activator, MK 5.1., exhibited increased rigidity, which impeded the mixing and embedding of the mixture into moulds). Precursors were mixed with an alkali activator Na-silicate solution (Geosil, 34417, Woelner, Germany; SiO₂ 27.5 m%, Na₂O 16.9 m%, H₂O 55.6 m%, where m% stands for mass percentage; SiO₂/Na₂O molar ratio 1.7, H₂O/Na₂O molar ratio 11.3) in ratios presented in Table 2. Mixtures were prepared by experimentally adjusting the activator content to achieve different workability levels of the slurry, from potentially too low to too high, to determine the optimal ratio (mixtures x.3 in Table 2) to avoid buoyancy and gain high compressive strength. Because buoyancy was not controlled solely by water, but also by the Na-silicate solution, the tendency for efflorescence was also affected.

Table 2. Mixture design of AAMs from precursors SA, GW, RW, FA, and MK with the mass ratio of precursor and activator, and viscosity of the fresh slurry (η).

Precursor Label	Mixture Label	$m_{\text{precursor}}$	$m_{\text{Na-silicate solution}}$	Mass Ratio	η
				Precursor to Activator	
		[g]	[g]	[/]	[Pa·s]
SA	1.1.	100	50	1:0.50	1.08
SA	1.2.	100	100	1:1.00	0 (severe foaming)
SA	1.3.	100	35	1:0.35	Torque overload
GW	2.1.	100	50	1:0.50	Torque overload
GW	2.2.	100	100	1:1.00	3.56
GW	2.3.	100	80	1:0.80	9.25
RW	3.1.	100	50	1:0.50	Torque overload
RW	3.2.	100	100	1:1.00	1.43
RW	3.3.	100	80	1:0.80	11.99
FA	4.1.	100	50	1:0.50	6.47
FA	4.2.	100	100	1:1.00	2.27
FA	4.3.	100	35	1:0.35	31.36
MK	5.1.	100	50	1:0.50	-
MK	5.2.	100	100	1:1.00	3.01
MK	5.3.	100	120	1:1.20	1.96

Workability was evaluated by measuring the viscosity (η ; Table 2) using a viscometer (Haake PK 100, VT 500 with detector PK2 1.0° at 25 °C, with plate–plate geometry of diameter 2 cm and distance between plates of 0.3 mm; with measurement protocol: 60 s upwards ramp (shear rate from 0.13 to 400 s⁻¹), 30 s hold time (shear rate 400 s⁻¹), and 60 s downwards ramp (shear rate from 400 to 0.13 s⁻¹). The lower the amount of liquid, the higher the viscosity. In selected cases, viscosity was not measurable (torque overload: the apparatus stopped when the torque value exceeded 115% of the maximum torque to protect against overload). In the case of mixture SA 1.2, the measured viscosity was 0 owing to severe foaming (when the amount of liquid alkali was higher, slag expressed self-foaming ability) [102,103].

The self-foaming effect observed only in the mixture SA 1.2 can be attributed to the initial ratio of amorphous Si:Al being 0.9, which is below 1.4. Namely, a 1.4 value, according to Duxsons et al. [102], is a ratio where geopolymer has a highly porous structure. Although the addition of Na-silicate solution increased the Si:Al ratio to the non-foaming ratio (for mixture SA 1.2, it is above 3, Table 3), this ratio is only the theoretical end-ratio of the structure and is neither local nor valid at any time during the dissolution and synthesis. To see foaming by the naked eye during the synthesis, the forces that are needed to contain the bubbles inside the structure should be weaker than the forces of gases formed inside the non-solid structure. In the case of mixture SA 1.2, the amount of alkali was the greatest, offering stronger dissolution and easier Brownian motion due to the highest amount of liquid phase, but at the same time, the highest amount of liquid phase leads to weaker forces that would be able to contain gases in the structure. A video of the self-foaming mixture SA 1.2 with no artificially induced motion (such as during measurement of viscosity, or while mixing) in a 12 mL plastic crucible is in the Supplementary Materials (Video S1).

Table 3. Molar ratios of elements potentially involved in alkali activation normalised to Al, and molar ratios of SiO₂ and H₂O normalised to elements from the 1st PS (material as whole and only the amorphous part); 1st PS and 2nd PS refer to elements from the 1st and 2nd groups of the periodic system, respectively.

Precursor Label	Mixture Label	1st PS/Al	2nd PS/Al	Si/Al	SiO ₂ /1st PS Whole	H ₂ O/1st PS Whole	SiO ₂ /1st PS Amorphous	H ₂ O/1st PS Amorphous
		[mol/mol]	[mol/mol]	[mol/mol]	[mol/mol]	[mol/mol]	[mol/mol]	[mol/mol]
SA	1.1.	1.36	2.61	2	2.04	5.66	1.48	5.68
SA	1.2.	2.71	2.61	3.14	1.44	5.66	1.16	5.66
SA	1.3.	0.95	2.61	1.66	2.54	5.63	1.74	5.63
GW	2.1.	5.92	2.48	10.47	1.77	2.15	1.77	2.19
GW	2.2.	8.21	2.48	12.4	1.51	3.12	1.51	3.16
GW	2.3.	7.3	2.48	11.63	1.60	2.81	1.59	2.85
RW	3.1.	0.91	1.54	2.27	2.48	4.31	2.50	4.40
RW	3.2.	1.61	1.54	2.86	1.77	4.90	1.77	4.95
RW	3.3.	1.33	1.54	2.62	1.98	4.74	1.98	4.80
FA	4.1.	0.98	0.57	2.16	2.71	4.36	2.21	4.52
FA	4.2.	1.76	0.57	2.81	1.89	4.93	1.60	5.02
FA	4.3.	0.75	0.57	1.96	3.41	4.14	2.63	4.14
MK	5.1.	0.47	0.02	1.45	3.68	5.22	3.05	5.22
MK	5.2.	0.91	0.02	1.81	2.32	5.44	1.99	5.44
MK	5.3.	1.08	0.02	1.96	2.08	5.48	1.82	5.48

The slurries of AAM mixtures were moulded in parallels in rubber–silicone $80 \times 20 \times 20 \text{ mm}^3$ moulds and cured in a heating chamber (WTB Binder, Binder GmbH, Tuttlingen, Germany) at $40 \text{ }^\circ\text{C}$ for 6 days, with gentle ventilation (10%) and open flap (10%), and not covered to allow all chemical and physical reactions to take place. The loss of water during curing is in the Supplementary Materials in Table S3. The prisms were demoulded after cooling to room temperature. On the 7th day, half of the cured samples were irradiated by microwaves in an inverter microwave oven (Gorenje microwave oven MO 17DV, Velenje, Slovenia; frequency 2.45 GHz, magnetron source) at 100 W. The dehydration process was conducted at 1 min intervals, with the total dehydration time adjusted based on visual observations of water condensation on a glass beaker covering the sample. The dehydration process was terminated when, after several repetitions of irradiation, no further condensation was observed on the beaker, indicating that the samples were fully dehydrated. Further, the presence of water was evaluated by FTIR measurement. The complete dehydration times of the samples with the percentage mass loss are shown in Supplementary Table S3.

2.4. Characterisation of AAMs

To evaluate the effects of microwave dehydration during the post-curing phase on the (non-)irradiated mechanically intact bulk AAMs, the following physical and chemical properties were analysed: mechanical strength and porosity (mercury intrusion porosimetry; MIP), chemical (FTIR), and mineralogical (XRD) composition. The porosity was also evaluated using SEM.

All AAM prisms, non-irradiated and microwave-dehydrated (before and after irradiation), were weighed, and their physical dimensions (height, width, and length) were measured on day 7. The 7-day-old geometric density of the AAMs was calculated by dividing the measured mass by the volume (Figure S2a).

The effect of irradiation was determined as loss of mass in the irradiated material (water evaporation), change in volume, and geometrical density, all calculated as the difference between the mass/volume/geometrical density ($\Delta m / \Delta V / \Delta \text{Geometrical density}$) of AAMs after and before dehydration, and normalised to mass/volume/geometrical density before dehydration (results are shown in Supplementary Table S3 and Figure S3).

The compressive strengths of three prisms for each mixture formulation (dehydrated and non-dehydrated) were measured on day 7 using a mechanical-strength testing machine (ToniTechnik ToniNORM, Berlin, Germany).

Destructed pieces of AAM prisms were milled (vibrating disk mill Siebtechnik TS250, Siebtechnik GmbH, Mülheim an der Ruhr, Germany) and sieved below $63 \text{ }\mu\text{m}$ for FTIR and XRD analysis (same instrument and setup as described in 2.1). Measurements were performed on 14-day-old and 1-year-old samples to observe the early irradiation effect, long-term evolution, and affinity of the material to water.

Non-destroyed pieces of the AAM prisms were further analysed by MIP (Micromeritics Autopore IV 9500) to evaluate the influence of forced microwave dehydration on the pore size distribution evolution. All samples were dried and kept until MIP measurement in a heating chamber (WTB Binder, Binder GmbH, Tuttlingen, Germany) at $70 \text{ }^\circ\text{C}$.

Microstructural investigation focused on the presence of efflorescence was performed on non-coated, non-destroyed pieces of AAMs: before and after dehydration on 7-day-old and 1-year-old samples, and before and after the application of a water droplet on 1-year-old-samples, using SEM under low-vacuum mode at an accelerating voltage of 20 kV. Energy-dispersive X-ray spectroscopy (EDXS, Link Pentafet, Oxford Instruments, Abingdon, UK) was used to evaluate the (potential) salt formation.

Selected 1-month-old pieces of the most chemically favourable mixture for the development of efflorescence were additionally exposed to a drop of distilled water and a drop of isopropyl alcohol, for a short-lasting macroscopic development investigation (Macro 5 MP 1/5'' sensor, f/2.4-aperture lens, 4 K, 60 fps video) of changes on the surface. The

samples were also immersed in distilled water and isopropyl alcohol (LabExpert, Ljubljana, Slovenia, 99.9%), and the pH and electrical conductivity (Mettler Toledo SevenDirect SD23, Columbus, OH, USA; pH: InLab Expert PRO-ISM, electrical conductivity (EC): InLab 731-ISM) of the solution were measured after 30 min, 24 h, and 14 days to determine the dissolution in different media.

3. Results and Discussion

3.1. Evaluation of AAMs

The theoretical potential of the mixtures presented in Table 2 to promote or prevent efflorescence was thoroughly examined.

3.1.1. Mixture Design Chemistry

According to the calculated molar ratios of the elements presented in Table 3 (containing only amorphous elements from the precursor and elements from the alkali–silicate solution), mixtures of 1.3, 3.1, 4.1, 4.3, and 5.2 did not theoretically facilitate the development of efflorescence, considering that the second group of PS does not contribute to the reaction. If the second group participates in the reaction, the only mixture that had the theoretical potential to avoid efflorescence was mixture 5.2. All the remaining mixtures had excess elements of the first (and second) group of the PS.

3.1.2. Macroscopic Observations of Efflorescence Formation and Response to Microwave Dehydration

Photographs of the 7-day-old non-dehydrated and microwave-dehydrated prisms are presented in Figure 4. The untreated alkali-activated prisms, which were not subjected to microwave dehydration, did not exhibit visible signs of efflorescence on day 7 (one day after the end of the curing treatment conducted at 40 °C). However, the prisms subjected to rapid complete dehydration through microwave irradiation displayed significant morphological alterations compared to their untreated counterparts. The changes were manifested as noticeable curvature, swelling, and surface cracking, where larger ‘surface’ cracks penetrated deep into the interior of the prisms (as in the case of μ 5.2 in Figure 4). The only exceptions wherein the external deformation was not significantly pronounced were the mixtures of RW prisms. The deformation of the microwave-treated samples was caused by internal pressures formed by the transformation of water from a liquid to a gaseous state, followed by rapid water removal from the prisms (and a decrease in internal pressure) through newly formed cracks.

The non-dehydrated prisms did not exhibit any visible signs of efflorescence after 7 days because of insufficient time for their development. Surface examination of the microwave-dehydrated prisms revealed bright spots formed when the unreacted alkali elements, which had failed to bind to the aluminosilicate network of the AAM over a given curing period of 7 days, were released by the transportation of steam out of the prism. These spots were most prominent on samples with a molar ratio of 1st PS/Al > 1, particularly in the mixtures denoted as μ 1.1, μ 2.1, μ 2.2, μ 2.3, μ 3.2, μ 3.3, μ 4.2, and μ 5.3 (Figure 4).



Figure 4. Photographs of the untreated and dehydrated prisms at day 7: (a1) untreated and (a2) dehydrated SA prisms; (b1) untreated and (b2) dehydrated GW prisms; (c1) untreated and (c2) dehydrated

RW prisms; (d1) untreated and (d2) dehydrated FA prisms; (e1) untreated and (e2) dehydrated MK prisms. Spots with visible signs of efflorescence are outlined with a red dotted line.

When the curing treatment at 40 °C for 6 days ended, water content was still present (Supplementary Table S3), and further reactions were still possible. In the case of microwave dehydration, removing the moisture immediately stopped any Brownian motion, freezing the reactions in time, and removing (part of) the unreacted alkali from the surface.

Photographs of the stored fragments exposed to ambient conditions for 30 days are presented in Figure S1. No additional efflorescence developed on the microwave-dehydrated samples after 30 days. This indicated the successful mitigation of efflorescence formation over a short-term period of 30 days under ambient-condition storage.

3.2. Mechanical Properties

The mechanical strengths of the untreated and microwave-dehydrated alkali-activated prisms are presented in Figure 5. A comparative examination of the compressive strengths of the various precursors used in this study revealed that GW and RW exhibited superior strengths, followed by FA, MK, and SA (general trend $GW > RW > FA > MK > SA$).

Under uniform curing conditions, the particle size of the precursors is an important factor influencing the compressive strength of AAM samples. The positive impact of smaller raw material particles used in alkali activation has a positive impact on the increased compressive strength [99], which is attributed to the larger reactive surface area in comparison to the volume. Consequently, a higher reaction rate of the precursor and more reacted final material is obtained. This is attributed to the larger reactive surface area in comparison to the volume, leading to a higher reaction rate of the precursor and more reacted final material [100]. Although the particle size is an important factor in the reactivity of AAMs, our observations indicated that other factors, such as the chemical composition of the amorphous content, physical properties, and mixture design, play critical roles in determining the compressive strength of the final product. The amorphous content of the precursor material is critical for AAM synthesis, as it directly affects the reactivity, dissolution, and subsequent formation of the aluminosilicate network. Therefore, the amorphous content of the precursor is a crucial parameter that significantly affects the mechanical properties of the AAMs [104]. In general, the presence of larger amounts of amorphous silica and alumina facilitates higher compressive strength of AAMs [101]. Nonetheless, the versatility of the results indicates that the only common physical parameter is the presence or absence of microwave irradiation.

In all the specimens, a visible decrease in compressive strength was observed upon post-curing microwave-induced dehydration treatment, with the noteworthy exception of mixtures 1.1 and 3.3. The compressive strength values remained comparable and exhibited a marginally less significant increase. The decline in compressive strength across the dehydrated samples was ascribed to the generation of cracks and the physical deterioration of the material structure during the heating reaction [90].

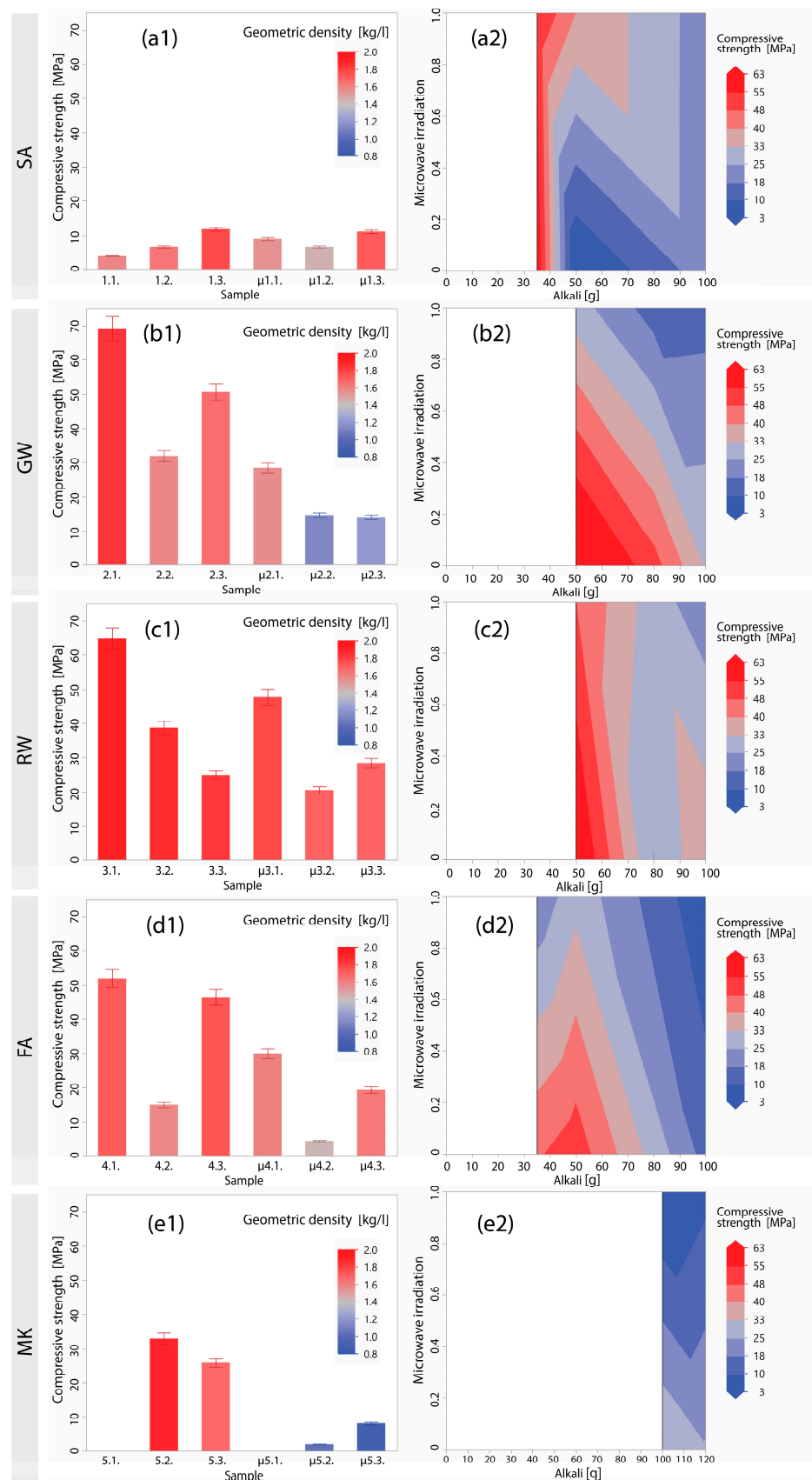


Figure 5. Compressive strengths and geometric densities of AAMs made from different precursors: (a1) SA, (b1) GW, (c1) RW, (d1) FA, (e1) MK. Each bar represents the compressive strength of a specific

mixture, while the bar colour indicates the geometric density of tested samples. Samples dehydrated with microwaves are marked with μ . Contour plots showing predicted compressive strengths with varying levels of low-power irradiation (1 on y-axis is 100 W) and alkali content: (a2) SA, (b2) GW, (c2) RW, (d2) FA, (e2) MK.

As represented in the contour plots in Figure 5 (right column), the optimum ratio between the chemistry of the material and the amount of alkali needed to dissolve the precursor (proper chemical mixture design avoiding efflorescence and aiming for the highest compressive strength [105]) was required to achieve the highest strength for each precursor. This is clearly evident in the case of FA (Figure 5d2), whereas all the others had the lowest ratio leading to efflorescence and the lowest amount of water. The decrease in compressive strength with an increase in microwave irradiation power was determined using Delauney triangulation up to 100 W, depending on the amount of liquid alkali (water and alkali content). In case of less water content, the decrease in compressive strength is smaller, which is logical; less water to be removed from the system implies the production of fewer cracks in the system and fewer imperfections that lead to lower mechanical performance.

The geometrical densities of untreated and microwave-dehydrated AAMs are presented in Figure 5a1–e1 as a colour scale and in Figure S2. Mechanical property analysis revealed a reduction in the compressive strength of the microwave-treated samples, primarily attributed to the decrease in geometric density, which is a consequence of newly formed cracks/pores in the irradiated AAMs.

Previous studies on the application of low-power microwave irradiation in the early stages of alkali activation typically resulted in enhanced compressive strength of AAMs owing to the instant increase in the temperature of the slurry and, therefore, the dissolution rate [53,84,106]. However, certain studies have demonstrated an increase in the compressive strength of alkali-activated fly ash with irradiation after conventional curing [107], with no explanation of the microwave used (the source of the microwaves [108], functioning of microwave in cyclic condition [108] or in continuous mode [109], what is the real-time of irradiation, the mass of irradiated sample, how much water it contained prior to irradiation [110], etc., which are all crucial parameters for repeating the experiment). Moreover, tests were performed only on one precursor without any definition for when a sample is ‘completely cured’ and material cannot develop further. In addition, there have been certain misleading conclusions on the use of microwave power, for instance that 100 W was not sufficient and that 300 W was the ‘dangerous’ power causing cracks, and the proper overall conclusion that lower microwave power required a longer time to reach the chosen temperature (and ‘level of completeness’ of curing) and higher power required less time, both depending on the mass and size of the specimen, and complete mass of the molecules that interact with the electromagnetic field.

Nonetheless, the present study showed that continuous microwave irradiation of hardened AAMs (that still contain a certain amount of water, 5–20 m%; Table S3) up to the point when there is no Brownian motion possible (water is removed from the system; Table S3 and FTIR evaluation in chapter 3.4) decreased the mechanical performance (Figure 5) owing to volumetrically induced porosity in the AAMs (Figures 4 and S4). This was further evaluated by MIP and SEM; even with only 100 W, we achieved destruction of the sample provided that the irradiation was ‘sufficiently long’ (Figure 6).

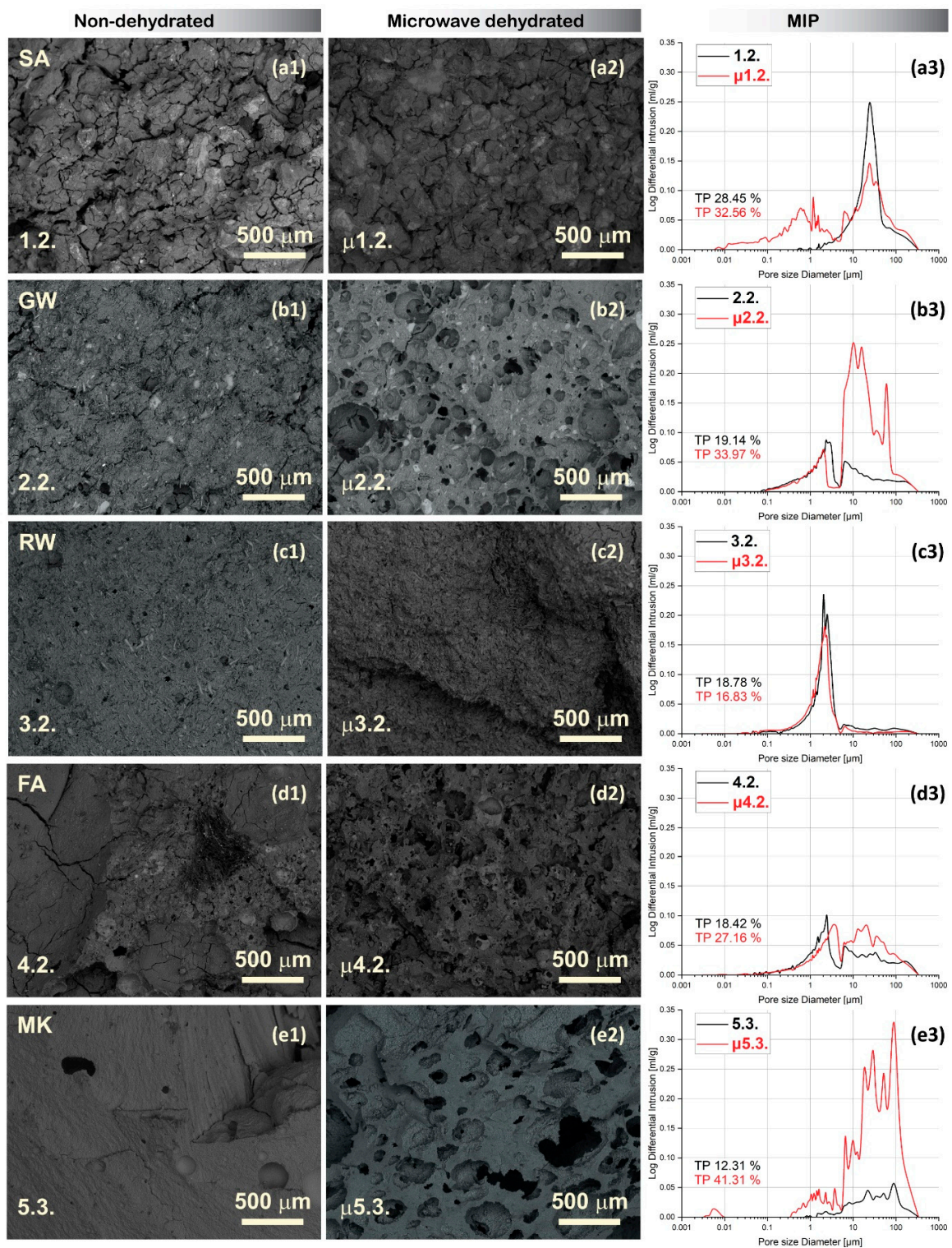


Figure 6. SEM micrographs (magnification 50 \times) and pore size distribution of samples with the highest amount of alkali solution per precursor and the highest probability for efflorescence development. Each row corresponds to a specific precursor: (a1) non-dehydrated SA, (a2) microwave-dehydrated SA, and (a3) pore size distribution of SA; (b1) non-dehydrated GW, (b2) microwave-dehydrated GW, and (b3) pore size distribution of GW; (c1) non-dehydrated RW, (c2) microwave-dehydrated RW, and (c3) pore size distribution of RW; (d1) non-dehydrated FA, (d2) microwave-dehydrated FA, and (d3) pore size distribution of FA; (e1) non-dehydrated MK, (e2) microwave-dehydrated MK, and (e3) pore size distribution of MK.

3.3. Microstructural Investigation

Figure 6 shows micrographs (magnification 50) of the selected mixture samples of each precursor, untreated and microwave-dehydrated, with the molar ratio that is most favourable for efflorescence development (molar ratio 1st PS/Al > 1; see Table 3), along with the corresponding pore size distributions determined by MIP. The pore distributions for all remaining samples are provided in Supplementary Figure S4, whereas the bulk and skeletal densities (also related to the compressive strength) are shown in Supplementary Figure S2.

While MIP analysis detected (entrances of) pores from 1 to 380 μm , further investigation through scanning microscopy unveiled the shape of formed pores and cracks, and the presence of larger pores and visible cracks within the microstructure of the microwave-treated samples. The total porosity increased with microwave irradiation, particularly when the mixture contained more water (Figure S4; less in mixtures 1.1 and 1.2, and more severely in mixtures 2.2, 2.3, 4.2, 5.2, and 5.3). Considering that every MIP measurement had an error of fragment selection, a small percentage of the difference in the total porosity was not relevant, unless the sample was non-homogeneous. However, from the MIP pore size distribution curve, it was only possible to conclude whether there was still any water present in the system attempting to break out owing to the irradiation-induced pressure unless there were no overall changes in the shape of the curve and total porosity (a few percentages of difference can be assigned to the choice of the fragment), as in the case of alkali-activated RW.

The geometric densities of the samples were lower than or comparable to those after dehydration. When the geometrical density was low, the samples were bloated and reshaped after irradiation, which increased the error in the measurement of dimensions (Figure S3), but this could still be used as an indicator of ‘completeness’ of curing. If volume increased after irradiation (Figure S3, green bars), the sample was not ‘completely’ cured (mixtures 2.1 (not that severe), 2.2, 2.3, 5.2, and 5.3).

However, neither MIP nor the geometrical density can be used to truly evaluate whether the samples were ‘completely’ cured (similarly, no Vicat test or any other tactile surface or surface-penetrating method used to evaluate the ‘rate of the reaction’). Nonetheless, as shown in Figure 6 (only the samples with the highest amounts of liquid alkali per precursor), SEM can reveal the shape and size of the pores, even those that are excessively large for MIP. In the microwave-treated samples, the newly formed microwave-induced pores manifested either as elongated cracks or spherical pores. Spherical pores can form only in the material that is still ‘soft’ and can be ‘squeezed’ on the inside without the ‘straight’ penetration to the surface. Spherical pores were present in samples 2.2, 4.2, and 5.3, for which the MIP indicated a significant increase in the total porosity. This yielded the conclusion that these materials required longer curing times or higher curing temperatures, which is not surprising, because the chosen curing temperature was low. In contrast, sample 3.2 demonstrated no changes under SEM or MIP, indicating that it was ‘completely’ cured. However, while sample 1.2 also did not show significant changes under SEM and total porosity, the pore size distribution changed from a monomodal to bimodal curve with the new peak ranging up to 10 μm , whereas the peak in irradiated and non-irradiated samples (ranging 10–300 μm) decreased. This indicated that the water present in the ‘completely’ cured sample exited the aluminosilicate network through newly created smaller-sized cracks. They slightly enlarged the volume of the aluminosilicate network ranging between larger cracks present in the non-irradiated sample, and pushed those larger cracks together. This can be confirmed through comparisons of SEM micrographs in Figure 6a1,a2. However, newly formed cracks and pores in microwave-irradiated AAMs negatively affect the mechanical properties and prevent the use of these materials for applications as load-bearing elements in construction. Nevertheless, they have the potential to be used as insulating materials if the new porosity is in the shape of closed spheres and not open cracks.

3.4. Influence of Microwave Dehydration on Mineralogy and Chemical Bonds Within the AAMs Along with Material Development

Several 7-day-old microwave-irradiated samples exhibited signs of alkaline mobility (as was also reported by [107]; Figure 4) on the surface as bright spots after irradiation (mixtures 1.1, 2.1, 2.2, 2.3, 3.2, 3.3, 4.2, and 5.3, which all have the highest amount of alkali liquid in the mixtures per precursor; Table 2). However, no signs of salt crystallisation or crystal phase changes owing to the evaporation of water were detected by XRD in the 14-day-old samples. This indicated that the local deposits were either amorphous or below the XRD-detection limit, as shown in Figure S5 (left) in the Supplementary Materials.

The FTIR spectra of 14-day-old AAMs depicted in Figure 7 (left) revealed no distinct changes in the structural chemistry of the aluminosilicate peak [111] of AAMs caused by the post-curing MW microwave treatment on day 7 (green square in Figure 7). The band in the range of 950–980 cm^{-1} , associated with the asymmetric stretching vibration band of T–O–Si (T = Al/Si), was similar for all samples. The major difference was in the broadband spanning 3000–3600 cm^{-1} (blue square in Figure 7). This region was assigned to O–H stretching vibrations [112], which were indicative of water molecules bound within the material matrix. Similarly, the peak at approximately 1640 cm^{-1} corresponded to the bending vibration of H–O–H [112], also indicative of water molecules (Figure 2). The absence of this band in the microwave-dehydrated samples indicated complete dehydration, suggesting that irradiation effectively reduced the water content within the materials. Consistent with broadband reduction and disappearance, the treated samples exhibited diminished peak intensities, which reinforced the suggestion of effective dehydration.

The band at 1420 cm^{-1} indicated the asymmetric stretching vibrations of C–O–C bonds in the carbonate ions (CO_3^{2-}). In the AAM samples made of the SA precursor, this band is particularly prominent, suggesting the significant presence of the carbonate phase (confirmed by XRD, Figure 2). Along with the peak at 874 cm^{-1} [113], which is also characteristic of carbonate vibrations, FTIR additionally proved the presence of calcite within the sample (measured by XRD, Figure 1).

However, there was a difference between the irradiated and non-irradiated 14-day-old samples made from SA in the band at 1420 cm^{-1} (Figure 7a1). The non-irradiated samples exhibited two peaks, the irradiated only one (the same peak exhibited by SA). Considering that SA has the highest ratio of amorphous elements from the second group of PS normalised to amorphous Al (Table 3) among all the used precursors (coupled with the fact that mixture 1.1 and 1.2 also have alkali elements in favour of efflorescence), and that non-dehydrated samples still contain water (allowing the movement of ions), the FTIR revealed early efflorescence development in the case of non-dehydrated 14-day-old SA (all mixtures, Figure 7a1). Considering that the non-dehydrated alkali-activated SA contained salts on its surface on day 30 (Figure S1a1), particularly sample 1.2, which had the largest left peak in the band at 1420 cm^{-1} (Figure 7a1) among non-dehydrated samples at 14 days, this additional peak was attributed to the efflorescence that could not be observed by the naked eye. Because the 14-day-old dehydrated counterparts did not have the ‘efflorescence’ peak (similar to no efflorescence observed on the 30-day-old irradiated SA samples), dehydration efficiently stopped efflorescence formation, that is, at least the rate of efflorescence formation in samples maintained at room temperature.

However, after 1 year, pulverised samples maintained at room temperature exhibited visible changes in the form of new peaks in the range of 1410–1500 cm^{-1} and at approximately 860 cm^{-1} (Figure 7, dashed squares). The peaks were more prominent in mixtures with higher alkali contents and were more pronounced in non-dehydrated samples. In contrast, in the microwave-dehydrated samples, the peaks were less pronounced and more commonly visible as smaller peaks (as in the case of μ 1.1 and μ 1.2) or enlarged bands (μ 1.3, μ 3.3, and μ 4.3). Following prolonged exposure of the samples to ambient conditions, moisture from the air and unreacted alkali allowed the local formation of crystalline efflorescence salts, as confirmed by XRD of the 1-year-old samples in Figure S5. In contrast, the 14-day-old samples did not show any newly formed crystalline phases.

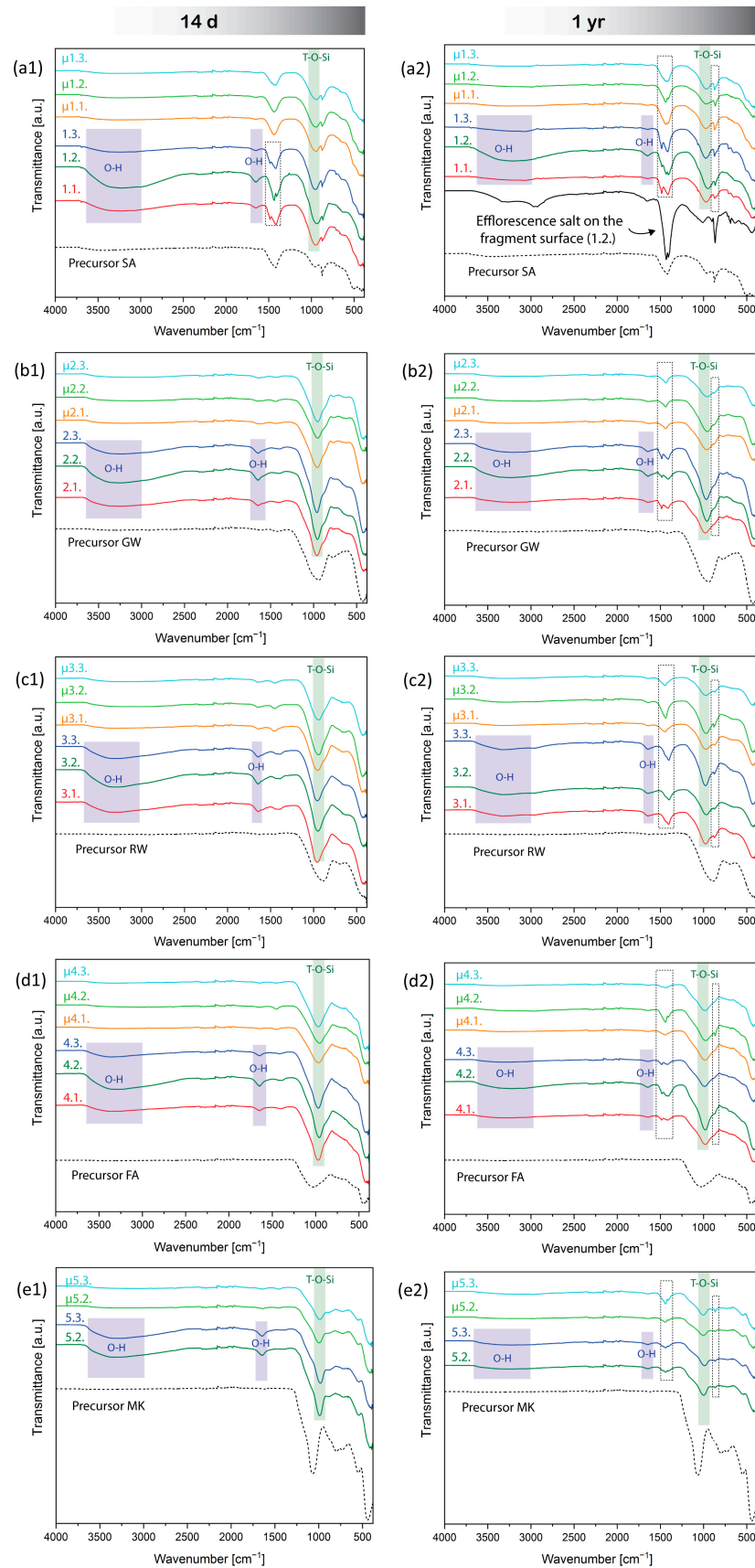


Figure 7. FTIR spectra of 14-day-old (left) and 1-year-old (right) AAMs made of: (a1,a2) SA, (b1,b2) GW, (c1,c2) RW, (d1,d2) FA, and (e1,e2) MK. Samples dehydrated with microwaves are marked

with μ . The dashed black line represents the precursor used for alkali activation, and the dashed grey line represents salt formed on the sample's surface after 1 year. The dashed square indicates visible differences indicating efflorescence formation.

Microwave dehydration successfully removed water from AAMs, as indicated by the absence of the spectral range of 3000–3600 cm^{-1} in the FTIR analysis presented in Figure 7. Together with the XRD analyses, no changes in the chemical bonds or formation of new crystalline phases were observed following the short term of 14 days (Figure S5 in the Supplementary Materials), rendering dehydration potentially useful for stopping the mineralogical reactions after 14 days.

3.5. Long-Term Observation of Dehydrated Samples and Induced Efflorescence Experiment

The 30-day-old non-dehydrated samples that were chemically inclined towards efflorescence showed naked-eye-visible efflorescence (Figure S1), and FTIR of 1-year-old alkali-activated SA samples (all mixtures) exposed to room temperature conditions (constant presence of moisture) showed clear development of the salts (Figure 7a2), regardless of the presence of dehydration. The inner structures were thoroughly examined using SEM, and the surfaces of the dehydrated samples were exposed to water droplets to observe the microstructural potential of salt formation (migration of alkali elements) (Figure 8).

Although signs of efflorescence were not macroscopically visible on microwave dehydrated samples after 1 year, 'inner' efflorescence, characterised by acicular or needle-like crystalline habitus, was observed in dehydrated mixtures 2.2, 4.2, and 5.3. Owing to rapid dehydration, the formation of microwave-induced cracks facilitated the permeability of moisture and air through the material; therefore, it was possible to locally determine the formation of Na salts (according to the EDXS results, they are part of the repository collection). This indicates that microwave dehydration is not an effective long-term method for preventing efflorescence formation under ambient storage conditions, because atmospheric moisture can rehydrate the samples, leading to salt formation inside the material. For the prolonged inhibition of efflorescence, it is recommended to store the samples in a vacuum- or humidity-free environment.

Upon reintroducing water onto the microwave-dehydrated AAM samples, Na instantly accumulated on the hydration sites, circularly on the surface of the hydrophobic MK mixture (irradiated 5.3, Figure 8e4, which is the first SEM micrograph of the hydrophobicity of the surface), in the surface cracks, which instantly absorbed water (irradiated mixtures from SA, 1.2, and FA, 4.2), and spread on the surface to the points of water contact (irradiated GW, 2.2, and RW, 3.2). The immediate appearance of Na on the AAM surface may cause slipperiness upon contact with water, rendering AAMs with improper mixture designs and without proper measures unsuitable for use as walking surfaces (pavements). Because (instant) slipperiness was also observed in our previous study on a geopolymer (made from MK and Na-silicate solution) with a mixture that theoretically did not lead to efflorescence [28], Na-alkali may not be the proper choice for alkalis in alkali-activated synthesis. Na is the smallest atom among the alkalis and is therefore loosely bonded in the structure and easily migrates in the aluminosilicate network. However, it also requires only one bond to compensate for its outer electron layer, whereas alkalis from the second group of the PS require two bonds, which immediately restrict the movement of larger alkali elements. Therefore, efflorescence and slipperiness can be avoided.

The experiment on induced efflorescence by hydration demonstrates that, despite arresting the reaction through microwave dehydration, the occurrence of efflorescence cannot be entirely prevented if the chemistry of the material remains unfavourable in the presence of moisture or water in the environment.

SEM–EDXS mapping for elements of the first and second groups of PS showed exclusive Na excretion at the surface upon induced efflorescence on the dehydrated samples after one year, as shown in Figure S6 in the Supplementary Materials.

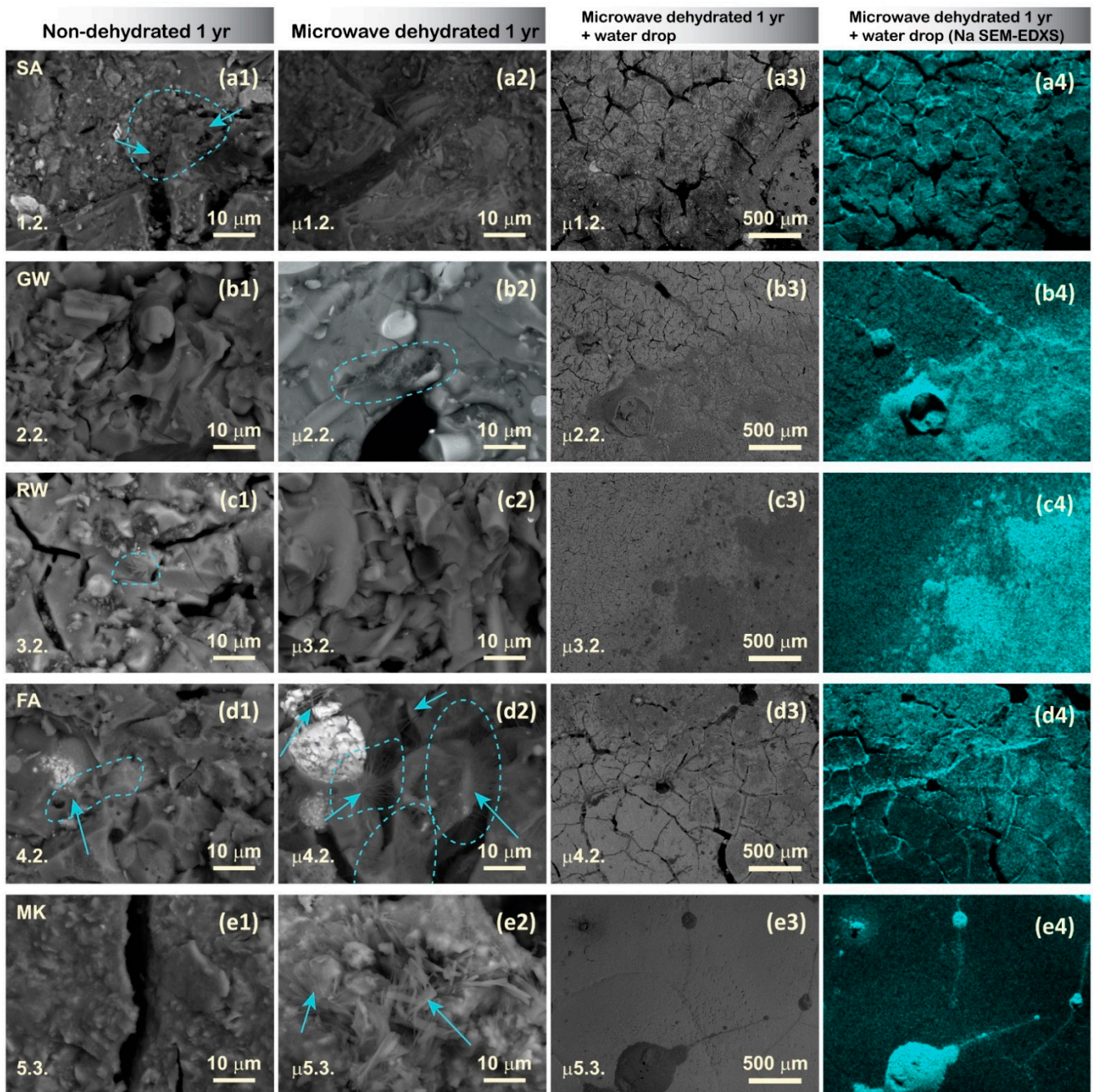


Figure 8. SEM micrographs and EDXS maps of samples with the highest amount of alkali solution per precursor and the highest probability for efflorescence development. Non-dehydrated samples are shown in the first column (a1–e1), microwave-dehydrated samples (μ) at $2000\times$ magnification in the second column (a2–e2), microwave-dehydrated samples at $50\times$ magnification in the third column (a3–e3), and EDXS maps indicating Na-appearance induced by a water droplet in the fourth column (a4–e4). Arrows and dashed boxes indicate microscopical spots of efflorescence salts.

Time observations of efflorescence induced by the addition of water to the outer surface of the 1-month-old most chemically favourable mixture for the development of efflorescence (2.2 according to the theoretical ratio of first group PS/Al, Table 3) are presented in Figure 9a. The addition of excessive alkali to the mixture resulted in an excess (free alkali). Consequently, a significantly higher level of alkalinity leaching was observed, which also indicated a greater tendency for efflorescence. The chemistry of solutions in AAMs, where the Na molar ratio exceeded that of Al, facilitated an excess of Na ions that

were not bound to the structure [114]. This could be observed by the naked eye 30 min after water droplet introduction (Figure 9a,c).

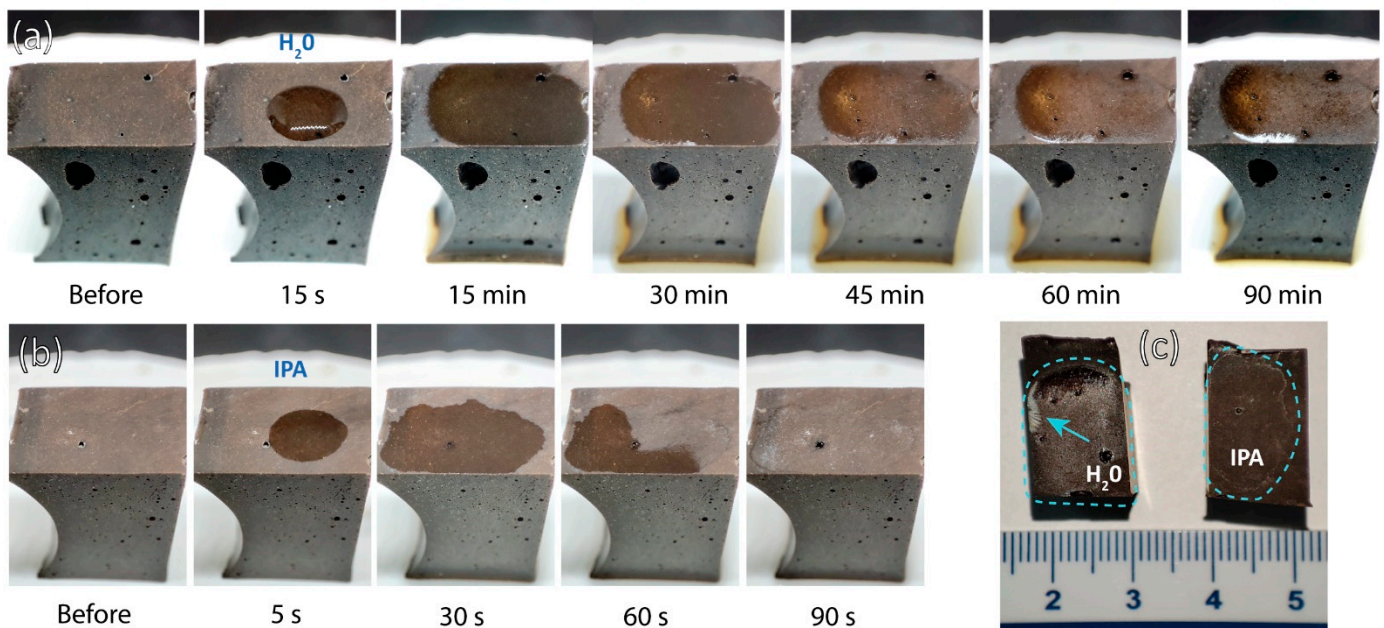


Figure 9. (a) Induced efflorescence formation over time after adding a drop of distilled water to the outer surface of sample 2.2. (b) Experiment with the addition of IPA to the surface of 2.2. (c) Inspection of the surface where distilled water and IPA have been added, with the edge of the dried droplet remaining visible. Dashed boxes indicate the edge of the dried droplet, and arrows point to visible early signs of efflorescence development.

When a drop of isopropanol (IPA) was added, rapid evaporation was observed, leaving white traces on the surface in the area of droplet contact after 60 s (Figure 9b,c). However, the effects of IPA on AAMs and geopolymers have not yet been thoroughly studied. The white traces may be the result of the formation of the first stages of efflorescence or the mobilisation of pre-existing efflorescence in the outermost layer of the overburden, which cannot yet be detected.

A detailed investigation of the visible edges of the dried droplets of distilled water and IPA (Figure 9c) is presented in Figure S7 in the Supplementary Materials.

Higher amounts of free alkalis also indicate a higher electrical conductivity (EC) of the solution [114], as shown in Figure 10, where the immersion of 2.2 (with excess alkali) in distilled water and IPA increased the EC over the immersion time. This increase was more pronounced in the case of distilled water, whereas it was still present after IPA immersion. Pure IPA, such as the 99.9% pure IPA used in the study, does not conduct electricity, as shown in Figure 8a. However, after immersion of the samples in IPA, the solution contained a small amount of ions, which can conduct to a certain extent. Distilled water, which has low conductivity of approximately $3 \mu\text{S}/\text{cm}$ (where deionised water has EC $0 \mu\text{S}/\text{cm}$), dissolves free alkalis and unbonded ions from the AAM sample. This results in a significant increase of EC and water solution colour intensity over time.

Detailed data on the electrical resistivity and temperature of the EC and pH probes are presented in Supplementary Table S4.

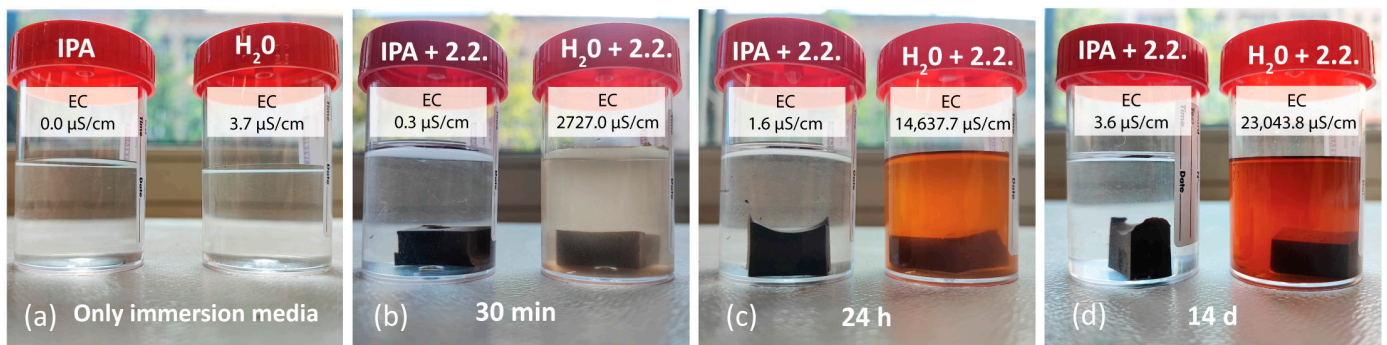


Figure 10. Immersion of sample 2.2 in different media over time: IPA left cup, distilled water right cup. In the case of immersion in water, the colour change of the solution is visible.

4. Conclusions

This study aimed to evaluate the influence of low-power microwave irradiation on conventionally cured few-day-old AAMs, with a focus on long-term efflorescence in worst-case-scenario mixtures. To draw an overall conclusion in the field of AAMs, the precursors used differed in all aspects: particle size and shape, chemistry, mineralogy, and amorphous content. In addition to using various precursors, AAMs were prepared with different mass ratios of precursor to Na-silicate solution to vary the chemistry (through the addition of Na and Si) and amount of water.

Although low-power microwave irradiation in the early stages of alkali activation usually boosts the compressive strength of AAMs owing to the instant increase in temperature and, therefore, the dissolution rate, the impact of irradiation on the compressive strength of hardened AAMs while boosting volumetric dehydration is aversive (up to a 72% decrease in the case of GW 2.3) and a non-reversible effect through an increase in porosity (up to a 29% increase in the case of MK 5.3). However, the microwave-induced porosity had two types of pore shapes: (i) elongated cracks and (ii) spheres. The first is formed in fully cured and hardened AAM, and the second is formed in AAM, which required additional time or a higher curing temperature. Therefore, microwave irradiation of AAMs can be used to determine whether AAM is completely cured, as well as to foam AAM, while avoiding the buoyancy of gases, which can result in volumetrically homogenous porosity and potentially useful building material as an insulator. However, AAMs that end with elongated cracks cannot be used for any purpose in building and civil engineering, not for load-bearing products (low mechanical strength) or for insulation (large, elongated, connected pores), regardless of whether the mixture had the potential to be efflorescence-free.

Nonetheless, the foaming of slow-curing AAMs can be performed only on AAMs that have alkali elements lower than the limit value to avoid salt formation. In addition, all crucial reactions should be near completion, implying that an increase in temperature provides the final boost to the curing procedure. However, the dehydration for foaming should not be complete to avoid the formation of elongated cracks.

Instant removal of water was achieved through pressure-created cracks using a volumetric heating approach. Along with water migrating out from the heated material, unreacted and unbonded alkali existed, which was observed as white stains on the surface of the AAM. The more efflorescence-favourable the mixture, the more obvious and prominent the white stains, which are the first signs of stopping chemical reactions. With time, salts formed on the surface of non-dehydrated, highly efflorescence-favourable mixtures (slag with the highest amount of alkali) after 1 month (detected by FTIR after 14 days), which further evolved in the powder form regardless of the (non-)dehydration. Dehydrated samples did not show efflorescence that would be visible to the naked eye even after 1 year when kept under room conditions (closed in plastic containers, but not air-tight); however, FTIR and XRD of 1-year old samples exhibited efflorescence. To perform chemical analysis on old, dehydrated samples, the samples should be kept under moisture-free conditions.

Because rapid dehydration opened the structure of AAM through elongated cracks, the 'outer surface' of AAM was now also on the inside of the AAM, easily approachable by air and moisture. Therefore, in 1-year-old samples made with excessive alkali (dehydrated mixtures 2.2, 4.2, 5.3), the formation of Na salts in the inner structure was observed. However, these salts were difficult to find, and thus they formed only locally.

Nonetheless, when water was introduced back into the dehydrated system that had the highest amount of alkali (as the droplet on the surface of the AAM), 'efflorescence' appeared as Na accumulated on the spot where water was applied. If the surface was hydrophobic, the Na stains were small circles; otherwise, they spread around the surface to the point where the water reached. If the surface had cracks, water penetrated the AAM and exposed Na in the cracks. Thus, the reactions were stopped; however, efflorescence could still form if conditions allowed (moisture in the environment or water).

The instant appearance of Na on the surface of the AAMs may be the cause of the instant slipperiness created when the AAM comes into contact with water. Thus, AAMs might not be useful for the walking surface (pavement) if proper measures are not introduced: a rough surface on the walking side of the AAM, sand throughout the entire volume or at least on the surface of AAM, AAM so porous that water penetrates instantly (heavy metal and toxic element leaching should be avoided), rubber on the surface of AAM, or any other type of surface modification. In addition, these results may require the replacement of Na-alkalis in AAMs with alkali elements from the second group of the PS, which are larger as atoms, need two bonds, and are therefore less mobile in the aluminosilicate network.

Therefore, the removal of water from intact bulk AAM prisms using volumetric heating can quickly and efficiently stop the chemical and mineralogical evolution of the material, whereas the irradiation itself does not influence the chemistry and mineralogy of AAM. In materials research, where the time evolution of samples follows, being able to physically freeze material-in-time is crucial for quality research.

Induced efflorescence and immersion tests with distilled water indicated that an improper mix design led to efflorescence and leaching. While IPA droplets and immersion may promote small changes in the material chemistry of AAMs, other methods of chemical reaction hindering, such as microwave dehydration, should be further investigated. However, polishing of AAM samples for SEM investigation should not be performed with water, as IPA can also induce changes on the surface of the polished sample.

Moreover, microwave-irradiation-induced dehydration instantly stopped efflorescence, which might represent a promising, time-efficient, cost-effective, solvent-free, and environmentally friendly alternative to the conventional mitigation of efflorescence for post-characterisation purposes of samples that are further maintained in a waterless environment. This method cannot be used for mitigating efflorescence in load-bearing products, but shows potential for the synthesis of permeable materials that could be used for filtration, adsorption, or even CO₂ capture.

Supplementary Materials: The following supporting information can be downloaded at: <https://www.mdpi.com/article/10.3390/min14121219/s1>, Table S1. XRD reference mineral cards and corresponding chemical formulas used for the analysis of XRD patterns of precursors with the amount of amorphous content.; Table S2. PSD summary for precursors SA, GW, RW, FA, and MK, including the mean diameter (MD) considering the volume of particles and main percentiles (d10, d50, and d90).; Table S3. Total dehydration time and mass owing due to the irradiation of 7-day-old AAM mixtures at a constant microwave power of 100 W. Initial amount of water in the slurry and loss of water owing to curing.; Figure S1. Fragments of prisms after mechanical properties testing on day 7, exposed to ambient conditions for 30 days.; Figure S2. Geometric, bulk, and skeletal densities of all prepared AAMs (a). Contour plot illustrating the relationship between bulk and skeletal density and their influence on compressive strength (b). Colour gradient (Delaunay triangulation) represents compressive strength, with red and blue indicating higher and lower strengths, respectively.; Figure S3. Effect of dehydration on mass, volume and geometrical density.; Figure S4. Pore size distribution of AAMs made of a) SA, b) GW, c) RW, d) FA, and e) MK. Total porosity (TP) is given as the proportion of pores to the volume of material. Samples dehydrated with microwaves are marked with μ .

Figure S5. The XRD patterns of 14-day-old (left) and 1-year-old (right) AAMs made of: a) SA, b) GW, c) RW, d) FA, and e) MK. Samples dehydrated with microwaves are marked with μ .; Figure S6. SEM-EDXS mapping on 1-year-old dehydrated samples for the elements sodium (Na), potassium (K), calcium (Ca) and magnesium (Mg).; Figure S7. SEM image of the remaining traces after droplet drying: (a) distilled water and (b) IPA, and EDXS spot analysis.; Table S4 Detailed data of electrical resistivity and temperature of EC and pH probes measuring immersion solution of sample 2.2. owing to difficulties in pH measurements of hydroalcoholic solutions, the pH values of IPA immersion solution are only arbitrary numbers and marked with *.; Video S1: The self-foaming effect of the mixture SA 1.2.; Video S2: The drying of a drop of distilled water on the surface of the sample GW 2.2 (video is sped up 10 x); Video S3: The drying of a drop of IPA on the surface of the sample GW 2.2. Refs. [115–117] are cited in the Supplementary Materials.

Author Contributions: Conceptualisation, A.T. and B.H.; data curation, A.T. and B.H.; formal analysis, A.T. and B.H.; funding acquisition, A.T. and B.H.; investigation, A.T. and B.H.; methodology, A.T. and B.H.; validation, A.T. and B.H.; visualisation, A.T. and B.H.; writing—original draft, A.T.; writing—review and editing, A.T. and B.H. All authors have read and agreed to the published version of the manuscript.

Funding: This study is part of Barbara Horvat’s ARIS project and was financially supported by the Slovenian Research Agency under Grant No. J2-3035.

Data Availability Statement: The original data presented in the study are openly available in the repository DiRROS at <http://hdl.handle.net/20.500.12556/DiRROS-20199>.

Acknowledgments: This study is part of Barbara Horvat’s ARIS project and was performed at the Slovenian National Building and Civil Engineering Institute while Horvat was still employed there, for which Horvat thanks the Institute. Horvat is grateful also to the Milan Vidmar Electric Power Research Institute for offering peer review, proofreading, and evaluation of the work by the committee. Anže Tesovnik is supported by the Young Researcher Program within the ARIS Program Group P2-0273, for the presented study he was financed from Barbara Horvat’s ARIS project.

Conflicts of Interest: The authors declare no conflicts of interest.

Abbreviations

AAM	Alkali-activated material
SA	Electric arc furnace slag
RW	Rock wool
GW	Glass wool
FA	Fly ash
MK	Metakaolin
μ	Dehydrated sample, with microwave irradiation

References

1. Damtoft, J.S.; Lukasik, J.; Herfort, D.; Sorrentino, D.; Gartner, E.M. Sustainable Development and Climate Change Initiatives. *Cem. Concr. Res.* **2008**, *38*, 115–127. [[CrossRef](#)]
2. Kourtit, K.; Nijkamp, P.; Scholten, H. The Future of the New Urban World. *Int. Plan. Stud.* **2015**, *20*, 4–20. [[CrossRef](#)]
3. Provis, J.L. Alkali-Activated Materials. *Cem. Concr. Res.* **2018**, *114*, 40–48. [[CrossRef](#)]
4. Barone, G.; Finocchiaro, C.; Lancellotti, I.; Leonelli, C.; Mazzoleni, P.; Sgarlata, C.; Stroschio, A. Potentiality of the Use of Pyroclastic Volcanic Residues in the Production of Alkali Activated Material. *Waste Biomass Valor* **2021**, *12*, 1075–1094. [[CrossRef](#)]
5. Santos, A.; Andrejkovičová, S.; Perná, I.; Almeida, F.; Rocha, F. Mechanical and Thermal Properties of Geopolymers Derived from Metakaolin with Iron Mine Waste. *Appl. Clay Sci.* **2024**, *258*, 107452. [[CrossRef](#)]
6. Ricciotti, L.; Occhicone, A.; Ferone, C.; Cioffi, R.; Tarallo, O.; Roviello, G. Sustainable Design of Geopolymer-Based Materials for Artistic and Restoration Applications. 2022. [[CrossRef](#)]
7. Viola, V.; D’Angelo, A.; Vertuccio, L.; Catauro, M. Metakaolin-Based Geopolymers Filled with Industrial Wastes: Improvement of Physicochemical Properties through Sustainable Waste Recycling. *Polymers* **2024**, *16*, 2118. [[CrossRef](#)]
8. Zhang, S.; Keulen, A.; Arbi, K.; Ye, G. Waste Glass as Partial Mineral Precursor in Alkali-Activated Slag/Fly Ash System. *Cem. Concr. Res.* **2017**, *102*, 29–40. [[CrossRef](#)]

9. Font, A.; Soriano, L.; de Moraes Pinheiro, S.M.; Tashima, M.M.; Monzó, J.; Borrachero, M.V.; Payá, J. Design and Properties of 100% Waste-Based Ternary Alkali-Activated Mortars: Blast Furnace Slag, Olive-Stone Biomass Ash and Rice Husk Ash. *J. Clean. Prod.* **2020**, *243*, 118568. [[CrossRef](#)]
10. Du, Y.; Pundienė, I.; Prancėvičienė, J.; Kligys, M.; Girskas, G.; Korjakins, A. A Review of Biomass Wood Ash in Alkali-Activated Materials: Treatment, Application, and Outlook. *J. Compos. Sci.* **2024**, *8*, 161. [[CrossRef](#)]
11. Novo, C.C.; Senff, L.; Seabra, M.P.; Novais, R.M.; Labrincha, J.A. The Role of an Industrial Alkaline Wastewater in the Alkali Activation of Biomass Fly Ash. *Appl. Sci.* **2022**, *12*, 3612. [[CrossRef](#)]
12. Mastali, M.; Zahra, A.; Hugo, K.; Faraz, R. Utilization of Mineral Wools in Production of Alkali Activated Materials. *Constr. Build. Mater.* **2021**, *283*, 122790. [[CrossRef](#)]
13. Fernández-Jiménez, A.; Cristelo, N.; Miranda, T.; Palomo, Á. Sustainable Alkali Activated Materials: Precursor and Activator Derived from Industrial Wastes. *J. Clean. Prod.* **2017**, *162*, 1200–1209. [[CrossRef](#)]
14. Setlak, K.; Mikuła, J.; Łach, M. Application of Industrial Waste Materials by Alkaline Activation for Use as Geopolymer Binders. *Materials* **2023**, *16*, 7651. [[CrossRef](#)] [[PubMed](#)]
15. Češnovar, M.; Traven, K.; Horvat, B.; Ducman, V. The Potential of Ladle Slag and Electric Arc Furnace Slag Use in Synthesizing Alkali Activated Materials; the Influence of Curing on Mechanical Properties. *Materials* **2019**, *12*, 1173. [[CrossRef](#)] [[PubMed](#)]
16. Li, Z.; Alfredo Flores Beltran, I.; Chen, Y.; Šavija, B.; Ye, G. Early-Age Properties of Alkali-Activated Slag and Glass Wool Paste. *Constr. Build. Mater.* **2021**, *291*, 123326. [[CrossRef](#)]
17. Horvat, B.; Pavlin, M.; Ducman, V. The Role of a Slag as a Co-Binder in Alkali-Activated Mineral Wool Waste. In Proceedings of the 7th Slag Valorisation Symposium, Leuven, Belgium, 27–29 April 2021; p. 6.
18. Awoyera, P.; Adesina, A. A Critical Review on Application of Alkali Activated Slag as a Sustainable Composite Binder. *Case Stud. Constr. Mater.* **2019**, *11*, e00268. [[CrossRef](#)]
19. Heshmat, M.; Amer, I.; Elgabbas, F.; Khalaf, M.A. Effect of Binder and Activator Composition on the Characteristics of Alkali-Activated Slag-Based Concrete. *Sci. Rep.* **2024**, *14*, 13502. [[CrossRef](#)]
20. Collins, F.; Sanjayan, J.G. Microcracking and Strength Development of Alkali Activated Slag Concrete. *Cem. Concr. Compos.* **2001**, *23*, 345–352. [[CrossRef](#)]
21. Gökçe, H.S. Durability of Slag-Based Alkali-Activated Materials: A Critical Review. *J. Aust. Ceram. Soc.* **2024**, *60*, 885–903. [[CrossRef](#)]
22. Palomo, A.; Grutzeck, M.W.; Blanco, M.T. Alkali-Activated Fly Ashes—A Cement for the Future. *Cem. Concr. Res.* **1999**, *29*, 1323–1329. [[CrossRef](#)]
23. Criado, M.; Vicent, M.; García-Ten, F.J. Reactivation of Alkali-Activated Materials Made up of Fly Ashes from a Coal Power Plant. *Clean. Mater.* **2022**, *3*, 100043. [[CrossRef](#)]
24. Maldonado-Alameda, A.; Mañosa, J.; Giro-Paloma, J.; Formosa, J.; Chimenos, J.M. Alkali-Activated Binders Using Bottom Ash from Waste-to-Energy Plants and Aluminium Recycling Waste. *Appl. Sci.* **2021**, *11*, 3840. [[CrossRef](#)]
25. Avila, Y.; Silva, R.V.; De Brito, J. Alkali-Activated Materials with Pre-Treated Municipal Solid Waste Incinerator Bottom Ash. *Appl. Sci.* **2022**, *12*, 3535. [[CrossRef](#)]
26. Deraman, L.M.; Kadir, A.A. Utilization of Bottom Ash for Alkali-Activated (Si-Ai) Materials: A Review. *J. Eng. Appl. Sci.* **2015**, *10*, 8351–8357.
27. Matsuda, A.; Maruyama, I.; Meawad, A.; Pareek, S.; Araki, Y. Reaction, Phases, and Microstructure of Fly Ash-Based Alkali-Activated Materials. *J. Adv. Concr. Technol.* **2019**, *17*, 93–101. [[CrossRef](#)]
28. Horvat, B.; Mušič, B. Waste Rubber Incorporated in the Alkali-Activated Metakaolin's Aluminosilicate Network Enhanced by Microwave Irradiation. In Proceedings of the 6th International Conference on Technologies & Business Models for Circular Economy: Conference Proceedings, Slovenia, Portorož, 6–8 September 2023.
29. Horvat, B.; Knez, N.; Hribar, U.; König, J.; Mušič, B. Thermal Insulation and Flammability of Composite Waste Polyurethane Foam Encapsulated in Geopolymer for Sustainable Building Envelope. *J. Clean. Prod.* **2024**, *446*, 141387. [[CrossRef](#)]
30. Valášková, M.; Klika, Z.; Vlček, J.; Matějová, L.; Topinková, M.; Pálková, H.; Madejová, J. Alkali-Activated Metakaolins: Mineral Chemistry and Quantitative Mineral Composition. *Minerals* **2022**, *12*, 1342. [[CrossRef](#)]
31. Chen, L.; Wang, Z.; Wang, Y.; Feng, J. Preparation and Properties of Alkali Activated Metakaolin-Based Geopolymer. *Materials* **2016**, *9*, 767. [[CrossRef](#)]
32. Pavlin, M.; Horvat, B.; Frankovič, A.; Ducman, V. Mechanical, Microstructural and Mineralogical Evaluation of Alkali-Activated Waste Glass and Stone Wool. *Ceram. Int.* **2021**, *47*, 15102–15113. [[CrossRef](#)]
33. Horvat, B.; Ducman, V. Influence of Particle Size on Compressive Strength of Alkali Activated Refractory Materials. *Materials* **2020**, *13*, 2227. [[CrossRef](#)]
34. Horvat, B.; Pavlin, A.S.; Ducman, V. Foundry Wastes as Potential Precursor in Alkali Activation Technology. In *Proceedings of the Technologies & Business Models for Circular Economy*; Univerzitetna založba Univerze v Mariboru/University of Maribor Press: Maribor, Slovenia, 2019.
35. Horvat, B.; Ducman, V.; Pavlin, A.S. Waste Foundry Sand as Precursor in Alkali Activation Process. *Livar. Vestn.* **2019**, *66*, 13.
36. Horvat, B.; Ducman, V. Potential of Green Ceramics Waste for Alkali Activated Foams. *Materials* **2019**, *12*, 3563. [[CrossRef](#)]
37. Žibret, L.; Wisniewski, W.; Horvat, B.; Božič, M.; Gregorc, B.; Ducman, V. Clay Rich River Sediments Calcined into Precursors for Alkali Activated Materials. *Appl. Clay Sci.* **2023**, *234*, 106848. [[CrossRef](#)]

38. Chen, B.; Wang, J. Experimental Study on the Durability of Alkali-Activated Slag Concrete after Freeze-Thaw Cycle. *Adv. Mater. Sci. Eng.* **2021**, *2021*, e9915639. [[CrossRef](#)]
39. Jin, L.; Huang, G.; Li, Y.; Zhang, X.; Ji, Y.; Xu, Z. Positive Influence of Liquid Sodium Silicate on the Setting Time, Polymerization, and Strength Development Mechanism of MSWI Bottom Ash Alkali-Activated Mortars. *Materials* **2021**, *14*, 1927. [[CrossRef](#)] [[PubMed](#)]
40. Liang, K.; Cui, K.; Sabri, M.M.S.; Huang, J. Influence Factors in the Wide Application of Alkali-Activated Materials: A Critical Review about Efflorescence. *Materials* **2022**, *15*, 6436. [[CrossRef](#)]
41. Longhi, M.A.; Zhang, Z.; Rodríguez, E.D.; Kirchheim, A.P.; Wang, H. Efflorescence of Alkali-Activated Cements (Geopolymers) and the Impacts on Material Structures: A Critical Analysis. *Front. Mater.* **2019**, *6*, 89. [[CrossRef](#)]
42. Longhi, M.A.; Rodríguez, E.D.; Walkley, B.; Zhang, Z.; Kirchheim, A.P. Metakaolin-Based Geopolymers: Relation between Formulation, Physicochemical Properties and Efflorescence Formation. *Compos. Part B Eng.* **2020**, *182*, 107671. [[CrossRef](#)]
43. Zhang, Z.; Provis, J.L.; Ma, X.; Reid, A.; Wang, H. Efflorescence and Subflorescence Induced Microstructural and Mechanical Evolution in Fly Ash-Based Geopolymers. *Cem. Concr. Compos.* **2018**, *92*, 165–177. [[CrossRef](#)]
44. Kim, H.-J.; Kang, S.-P.; Choe, G. Effect of Red Mud Content on Strength and Efflorescence in Pavement Using Alkali-Activated Slag Cement. *Int. J. Concr. Struct. Mater.* **2018**, *12*, 18. [[CrossRef](#)]
45. Yao, X.; Yang, T.; Zhang, Z. Compressive Strength Development and Shrinkage of Alkali-Activated Fly Ash–Slag Blends Associated with Efflorescence. *Mater. Struct.* **2016**, *49*, 2907–2918. [[CrossRef](#)]
46. Srinivasamurthy, L.; Chevali, V.S.; Zhang, Z.; Wang, H. Phase Changes under Efflorescence in Alkali Activated Materials with Mixed Activators. *Constr. Build. Mater.* **2021**, *283*, 122678. [[CrossRef](#)]
47. Cousture, A.; Renault, N.; Ndiaye, K.; Gallias, J.-L. New Binder Resulting from Alkali-Activation of Calcareous Components. In Proceedings of the 11th ACI/RILEM International Conference on Cementitious Materials and Alternative Binders for Sustainable Concrete, Online, 7–10 June 2021.
48. Li, M.; Huang, G.; Cui, Y.; Wang, B.; Zhang, S.; Wang, Q.; Feng, J. Improvement of Mechanical Properties and Condensation Behavior for Alkali-Activated Materials by Sodium Silicate. *Crystals* **2022**, *12*, 1018. [[CrossRef](#)]
49. Jia, R.; Wang, Q.; Luo, T. Deterioration and Mitigation of Efflorescence of Alkali-Activated Phosphorus Slag. *Constr. Build. Mater.* **2023**, *407*, 133500. [[CrossRef](#)]
50. Dow, C.; Glasser, F.P. Calcium Carbonate Efflorescence on Portland Cement and Building Materials. *Cem. Concr. Res.* **2003**, *33*, 147–154. [[CrossRef](#)]
51. Longhi, M.A.; Zhang, Z.; Walkley, B.; Rodríguez, E.D.; Kirchheim, A.P. Strategies for Control and Mitigation of Efflorescence in Metakaolin-Based Geopolymers. *Cem. Concr. Res.* **2021**, *144*, 106431. [[CrossRef](#)]
52. Nedeljković, M.; Ghiassi, B.; van der Laan, S.; Li, Z.; Ye, G. Effect of Curing Conditions on the Pore Solution and Carbonation Resistance of Alkali-Activated Fly Ash and Slag Pastes. *Cem. Concr. Res.* **2019**, *116*, 146–158. [[CrossRef](#)]
53. Horvat, B.; Pavlin, M.; Ducman, V. Influence of Microwaves in the Early Stage of Alkali Activation on the Mechanical Strength of Alkali-Activated Materials. *Ceram. Int.* **2023**, *49*, 24246–24258. [[CrossRef](#)]
54. Hsu, C.-H.; Chan, H.-Y.; Chang, M.-H.; Liu, C.-F.; Liu, T.-Y.; Chiu, K.-C. Efficient Compressive Strength Prediction of Alkali-Activated Waste Materials Using Machine Learning. *Materials* **2024**, *17*, 3141. [[CrossRef](#)]
55. Zhang, Z.; Provis, J.L.; Reid, A.; Wang, H. Fly Ash-Based Geopolymers: The Relationship between Composition, Pore Structure and Efflorescence. *Cem. Concr. Res.* **2014**, *64*, 30–41. [[CrossRef](#)]
56. Common X-Ray Tube Failure Modes. Available online: <https://www.spellmanhv.com/en/Technical-Resources/Application-Notes-X-Ray-Generators/AN-02> (accessed on 25 April 2024).
57. Saraya, M.E.I. Stopping of Cement Hydration by Various Methods. *HBRC J.* **2010**, *6*, 46–58.
58. Mezhev, A.; Kulisch, D.; Goncharov, A.; Zhutovsky, S. A Comparative Study of Factors Influencing Hydration Stoppage of Hardened Cement Paste. *Sustainability* **2023**, *15*, 1080. [[CrossRef](#)]
59. Zhang, Z.; Scherer, G.W. Physical and Chemical Effects of Isopropanol Exchange in Cement-Based Materials. *Cem. Concr. Res.* **2021**, *145*, 106461. [[CrossRef](#)]
60. Snellings, R.; Chwast, J.; Cizer, Ö.; De Belie, N.; Dhandapani, Y.; Durdzinski, P.; Elsen, J.; Haufe, J.; Hooton, D.; Patapy, C.; et al. RILEM TC-238 SCM Recommendation on Hydration Stoppage by Solvent Exchange for the Study of Hydrate Assemblages. *Mater. Struct.* **2018**, *51*, 172. [[CrossRef](#)]
61. Snellings, R.; Chwast, J.; Cizer, Ö.; De Belie, N.; Dhandapani, Y.; Durdzinski, P.; Elsen, J.; Haufe, J.; Hooton, D.; Patapy, C.; et al. Report of TC 238-SCM: Hydration Stoppage Methods for Phase Assemblage Studies of Blended Cements—Results of a Round Robin Test. *Mater. Struct.* **2018**, *51*, 111. [[CrossRef](#)]
62. Kakali, G.; Tsivilis, S.; Aggeli, E.; Bati, M. Hydration Products of C3A, C3S and Portland Cement in the Presence of CaCO₃. *Cem. Concr. Res.* **2000**, *30*, 1073–1077. [[CrossRef](#)]
63. Mitchell, L.; Margeson, J. The Effects of Solvents on C–S–H as Determined by Thermal Analysis. *J. Therm. Anal. Calorim.* **2006**, *86*, 591–594. [[CrossRef](#)]
64. Beaudoin, J.J.; Gu, P.; Marchand, J.; Tamtsia, B.; Myers, R.E.; Liu, Z. Solvent Replacement Studies of Hydrated Portland Cement Systems: The Role of Calcium Hydroxide. *Adv. Cem. Based Mater.* **1998**, *8*, 56–65. [[CrossRef](#)]
65. Yang, K.; White, C.E. Multiscale Pore Structure Determination of Cement Paste via Simulation and Experiment: The Case of Alkali-Activated Metakaolin. *Cem. Concr. Res.* **2020**, *137*, 106212. [[CrossRef](#)]

66. Zhang, Q.; Ye, G. Dehydration Kinetics of Portland Cement Paste at High Temperature. *J. Therm. Anal. Calorim.* **2012**, *110*, 153–158. [[CrossRef](#)]
67. Xu, L.; Wang, J.; Li, K.; Hao, T.; Li, Z.; Li, L.; Ran, B.; Du, H. New Insights on Dehydration at Elevated Temperature and Rehydration of GGBS Blended Cement. *Cem. Concr. Compos.* **2023**, *139*, 105068. [[CrossRef](#)]
68. Blog, B. Fundamentals of Heat Transfer. Available online: <https://www.boydcorp.com/blog/heat-transfer-fundamentals.html> (accessed on 9 November 2024).
69. Slongo, J.S.; Gund, J.; Passarin, T.A.R.; Pipa, D.R.; Ramos, J.E.; Arruda, L.V.; Junior, F.N. Effects of Thermal Gradients in High-Temperature Ultrasonic Non-Destructive Tests. *Sensors* **2022**, *22*, 2799. [[CrossRef](#)] [[PubMed](#)]
70. Matsunaga, N.; Kawaji, S.; Nanno, I.; Tanaka, M. A Novel Approach to Temperature Uniformity for Thermal Process. In Proceedings of the 2004 5th Asian Control Conference (IEEE Cat. No. 04EX904), Melbourne, VIC, Australia, 20–23 July 2004.
71. Fernandez, Y.; Arenillas, A.; Angel, J. Microwave Heating Applied to Pyrolysis. In *Advances in Induction and Microwave Heating of Mineral and Organic Materials*; Grundas, S., Ed.; InTech: Houston, TX, USA, 2011; ISBN 978-953-307-522-8.
72. English, N.J.; MacElroy, J.M.D. Molecular Dynamics Simulations of Microwave Heating of Water. *J. Chem. Phys.* **2003**, *118*, 1589–1592. [[CrossRef](#)]
73. Marracino, P.; Liberti, M.; d’Inzeo, G.; Apollonio, F. Water Response to Intense Electric Fields: A Molecular Dynamics Study. *Bioelectromagnetics* **2015**, *36*, 377–385. [[CrossRef](#)]
74. Drab, M.; Gongadze, E.; Mesarec, L.; Kralj, S.; Kralj-Iglic, V.; Igljč, A. The Internal and External Dipole Moment of a Water Molecule and Orientational Ordering of Water Dipoles in an Electric Double Layer. *Elektrotehniški Vestn.* **2017**, *84*, 221–234.
75. Qin, M.; Zhang, L.; Wu, H. Dielectric Loss Mechanism in Electromagnetic Wave Absorbing Materials. *Adv. Sci.* **2022**, *9*, 2105553. [[CrossRef](#)]
76. Lunkenheimer, P.; Emmert, S.; Gulich, R.; Köhler, M.; Wolf, M.; Schwab, M.; Loidl, A. Electromagnetic-Radiation Absorption by Water. *Phys. Rev. E* **2017**, *96*, 062607. [[CrossRef](#)]
77. Novotný, M.; Šuhajda, K.; Sobotka, J.; Gintar, J. Use of EMW Radiation in the Building Industry. *Adv. Mater. Res.* **2014**, *1041*, 297–302. [[CrossRef](#)]
78. Sobotka, J.; Smolka, R. Use of EMW Radiation in the Building Industry at Defects in Buildings. *MATEC Web Conf.* **2017**, *93*, 01008. [[CrossRef](#)]
79. Sobotka, J.; Kolář, R. Drying of the Basement Spaces of the Faculty of Arts in Brno. *Appl. Mech. Mater.* **2017**, *861*, 295–302. [[CrossRef](#)]
80. Jastrzębska, M. Ppractical application of the microwave oven in the geotechnical laboratory. *Archit. Civ. Eng. Environ.* **2019**, *12*, 91–104. [[CrossRef](#)]
81. Sobotka, J.; Smolka, R. Thermal Performance of Wooden Elements Exposed to Microwave Radiation during Treatment of Building Defects. *MATEC Web Conf.* **2019**, *279*, 02012. [[CrossRef](#)]
82. Hong, S.; Kim, H. Robust Synthesis of Coal Bottom Ash-Based Geopolymers Using Additional Microwave Heating and Curing for High Compressive Strength Properties. *Korean J. Chem. Eng.* **2019**, *36*, 1164–1171. [[CrossRef](#)]
83. Kim, H.; Hong, S. Rapid Compressive Strength Achievement of Coal Bottom Ash Based Geopolymer by Employing Microwave Energy. *TechConnect Briefs* **2018**, *2*, 215–218.
84. Hong, S.; Kim, H. Effects of Microwave Energy on Fast Compressive Strength Development of Coal Bottom Ash-Based Geopolymers. *Sci. Rep.* **2019**, *9*, 15694. [[CrossRef](#)] [[PubMed](#)]
85. Guan, X.; Luo, W.; Liu, S.; Hernandez, A.G.; Do, H.; Li, B. Ultra-High Early Strength Fly Ash-Based Geopolymer Paste Cured by Microwave Radiation. *Dev. Built Environ.* **2023**, *14*, 100139. [[CrossRef](#)]
86. Saxena, S.K.; Kumar, M.; Singh, N.B. Influence of Alkali Solutions on Properties of Pond Fly Ash-Based Geopolymer Mortar Cured under Different Conditions. *Adv. Cem. Res.* **2018**, *30*, 1–7. [[CrossRef](#)]
87. Graytee, A.; Sanjayan, J.G.; Nazari, A. Development of a High Strength Fly Ash-Based Geopolymer in Short Time by Using Microwave Curing. *Ceram. Int.* **2018**, *44*, 8216–8222. [[CrossRef](#)]
88. Onutai, S.; Jiemsirilera, S.; Thavorniti, P.; Kobayashi, T. Fast Microwave Syntheses of Fly Ash Based Porous Geopolymers in the Presence of High Alkali Concentration. *Ceram. Int.* **2016**, *42*, 9866–9874. [[CrossRef](#)]
89. Madsen, I.; Scarlett, N.; Kern, A. Description and Survey of Methodologies for the Determination of Amorphous Content Via X-Ray Powder Diffraction. *Z. Krist.* **2011**, *226*, 944–955. [[CrossRef](#)]
90. Heiri, O.; Lotter, A.F.; Lemcke, G. Loss on Ignition as a Method for Estimating Organic and Carbonate Content in Sediments: Reproducibility and Comparability of Results. *J. Paleolimnol.* **2001**, *25*, 101–110. [[CrossRef](#)]
91. Vdovin, K.N.; Pivovarova, K.G.; Ponamareva, T.B.; Feoktistov, N.A. Determination of Chemically Bound Water in Metakaolin. *Refract. Ind. Ceram.* **2019**, *59*, 654–657. [[CrossRef](#)]
92. Hajji, S.; Turki, T.; Boubakri, A.; Ben Amor, M.; Mzoughi, N. Study of Cadmium Adsorption onto Calcite Using Full Factorial Experiment Design. *Desalin. Water Treat.* **2017**, *83*, 222–233. [[CrossRef](#)]
93. Reig, F.B.; Adelantado, J.V.G.; Moya Moreno, M.C.M. FTIR Quantitative Analysis of Calcium Carbonate (Calcite) and Silica (Quartz) Mixtures Using the Constant Ratio Method. Application to Geological Samples. *Talanta* **2002**, *58*, 811–821. [[CrossRef](#)] [[PubMed](#)]
94. Gao, X.; Yu, Q.L.; Brouwers, H.J.H. Reaction Kinetics, Gel Character and Strength of Ambient Temperature Cured Alkali Activated Slag-Fly Ash Blends. *Constr. Build. Mater.* **2015**, *80*, 105–115. [[CrossRef](#)]

95. Criado, M.; Fernández-Jiménez, A.; Palomo, A. Alkali Activation of Fly Ash: Effect of the SiO₂/Na₂O Ratio. *Microporous Mesoporous Mater.* **2007**, *106*, 180–191. [[CrossRef](#)]
96. Agarwal, A.; Tomozawa, M. Correlation of Silica Glass Properties with the Infrared Spectra. *J. Non-Cryst. Solids* **1997**, *209*, 166–174. [[CrossRef](#)]
97. Prasad, I.; Chandorkar, A. Spectroscopy of Silicon Dioxide Films Grown under Negative Corona Stress. *J. Appl. Phys.* **2003**, *94*, 2308–2310. [[CrossRef](#)]
98. Zhang, Z.; Wang, H.; Provis, J.L. Quantitative Study of the Reactivity of Fly Ash in Geopolymerization by FTIR. *J. Sustain. Cem.-Based Mater.* **2012**, *1*, 154–166. [[CrossRef](#)]
99. Walkley, B.; Nicolas, R.S.; Sani, M.-A.; Gehman, J.D.; van Deventer, J.S.J.; Provis, J.L. Phase Evolution of Na₂O–Al₂O₃–SiO₂–H₂O Gels in Synthetic Aluminosilicate Binders. *Dalton Trans.* **2016**, *45*, 5521–5535. [[CrossRef](#)]
100. Sitarz, M.; Mozgawa, W.; Handke, M. Vibrational Spectra of Complex Ring Silicate Anions—Method of Recognition. *J. Mol. Struct.* **1997**, *404*, 193–197. [[CrossRef](#)]
101. Gao, L.; Zheng, Y.; Tang, Y.; Yu, J.; Yu, X.; Liu, B. Effect of Phosphoric Acid Content on the Microstructure and Compressive Strength of Phosphoric Acid-Based Metakaolin Geopolymers. *Heliyon* **2020**, *6*, e03853. [[CrossRef](#)] [[PubMed](#)]
102. Duxson, P.; Provis, J.L.; Lukey, G.C.; Mallicoat, S.W.; Kriven, W.M.; van Deventer, J.S.J. Understanding the Relationship between Geopolymer Composition, Microstructure and Mechanical Properties. *Colloids Surf. A Physicochem. Eng. Asp.* **2005**, *269*, 47–58. [[CrossRef](#)]
103. Tsaousi, G.-M.; Panias, D. Production, Properties and Performance of Slag-Based, Geopolymer Foams. *Minerals* **2021**, *11*, 732. [[CrossRef](#)]
104. Kamseu, E.; Alzari, V.; Nuvoli, D.; Sanna, D.; Lancellotti, I.; Mariani, A.; Leonelli, C. Dependence of the Geopolymerization Process and End-Products to the Nature of Solid Precursors: Challenge of the Sustainability. *J. Clean. Prod.* **2021**, *278*, 123587. [[CrossRef](#)]
105. Duxson, P.; Mallicoat, S.W.; Lukey, G.C.; Kriven, W.M.; van Deventer, J.S.J. The Effect of Alkali and Si/Al Ratio on the Development of Mechanical Properties of Metakaolin-Based Geopolymers. *Colloids Surf. A Physicochem. Eng. Asp.* **2007**, *292*, 8–20. [[CrossRef](#)]
106. Sun, Y.; Zhang, P.; Hu, J.; Liu, B.; Yang, J.; Liang, S.; Xiao, K.; Hou, H. A Review on Microwave Irradiation to the Properties of Geopolymers: Mechanisms and Challenges. *Constr. Build. Mater.* **2021**, *294*, 123491. [[CrossRef](#)]
107. Khaleel, F.; Atiş, C.; Durak, U.; İlkentapar, S.; Karahan, O. The Effect of Microwave Curing on the Strength Development of Class-F Fly Ash-Based Geopolymer Mortar. *Erciyes Üniversitesi Fen Bilim. Enstitüsü Fen Bilim. Derg.* **2021**, *37*, 118–129.
108. Elite RF. The Evolution of Microwave: From Magnetrons to Solid-State Generators. Available online: <https://eliterfllc.com/solid-state-vs-magnetrons/> (accessed on 10 November 2024).
109. What Is an Inverter Microwave and Is It Worth It? Available online: <https://www.choice.com.au/home-and-living/kitchen/microwaves/articles/what-is-an-inverter-microwave> (accessed on 10 November 2024).
110. Hu, Q.; He, Y.; Wang, F.; Wu, J.; Ci, Z.; Chen, L.; Xu, R.; Yang, M.; Lin, J.; Han, L.; et al. Microwave Technology: A Novel Approach to the Transformation of Natural Metabolites. *Chin Med* **2021**, *16*, 87. [[CrossRef](#)]
111. Vempati, R.K.; Rao, A.; Hess, T.R.; Cocke, D.L.; Lauer, J. Fractionation and Characterization of Texas Lignite Class F Fly Ash by XRD, TGA, FTIR and SFM. *Cem. Concr. Res.* **1994**, *24*, 1153–1164. [[CrossRef](#)]
112. Mojet, B.; Ebbesen, S.; Lefferts, L. ChemInform Abstract: Light at the Interface: The Potential of Attenuated Total Reflection Infrared Spectroscopy for Understanding Heterogeneous Catalysis in Water. *Chem. Soc. Rev.* **2010**, *39*, 4643–4655. [[CrossRef](#)] [[PubMed](#)]
113. Cai, G.-B.; Chen, S.; Liu, L.; Jiang, J.; Yao, H.-B.; Xu, A.-W.; Yu, S.-H. 1,3-Diamino-2-Hydroxypropane-N,N,N',N'-Tetraacetic Acid Stabilized Amorphous Calcium Carbonate: Nucleation, Transformation and Crystal Growth. *Crystengcomm* **2010**, *12*, 234–241. [[CrossRef](#)]
114. Kioupis, D.; Tsivilis, S. Alkali Leaching Control of Construction and Demolition Waste Based Geopolymers. *MATEC Web Conf.* **2018**, *149*, 01064. [[CrossRef](#)]
115. Simão, L.; Hotza, D.; Raupp-Pereira, F.; Ribeiro, M.; Montedo, O.; Fernandes, É. Controlling efflorescence in geopolymers: A new approach. *Case Stud. Constr. Mater.* **2021**, *15*, e00740. [[CrossRef](#)]
116. Fořt, J.; Mildner, M.; Keppert, M.; Černý, R. Waste solidified alkalis as activators of aluminosilicate precursors: Functional and environmental evaluation. *J. Build. Eng.* **2022**, *54*, 104598. [[CrossRef](#)]
117. Abbas-Ghaleb, R.; Chlala, D. Catalytic oxidation of isopropyl alcohol over platinum based catalyst: A study of the effect of methyl cellulose on Pt particles dispersion over mullite. *Braz. J. Chem. Eng.* **2019**, *36*, 1175–1184. [[CrossRef](#)]

Disclaimer/Publisher's Note: The statements, opinions and data contained in all publications are solely those of the individual author(s) and contributor(s) and not of MDPI and/or the editor(s). MDPI and/or the editor(s) disclaim responsibility for any injury to people or property resulting from any ideas, methods, instructions or products referred to in the content.